PARTIAL DIFFERENTIAL EQUATION MODELS FOR INTRANUCLEAR DIFFUSION, INVERSE PROBLEMS IN NANOBIOLOGY AND CELL CYCLE SPECIFIC EFFECTS OF ANTICANCER DRUGS

By

Peter Hinow

Dissertation

Submitted to the Faculty of the

Graduate School of Vanderbilt University

in partial fulfillment of the requirements

for the degree of

DOCTOR OF PHILOSOPHY

in

Mathematics

August, 2007

Nashville, Tennessee

Approved:

Professor Glenn F. Webb

Professor Mary Ann Horn

Professor Jennifer A. Pietenpol

Professor Philip S. Crooke

Professor Gieri Simonett

To my family

Ingeborg and Georg,

Martin and Iza,

and Yuqiang

ACKNOWLEDGMENTS

It is a great pleasure to offer my best thanks to all my teachers, collaborators and friends who have accompanied me over the past five years and without whom this thesis could not have been completed. First and foremost I want to thank my thesis adviser, Dr. Glenn F. Webb for his unwavering encouragement and support. Throughout the time that I had the privilege to work with him, Glenn always had an open ear and offered all his assistance. Many thanks go to the members of my doctoral committee, Drs. Mary Ann Horn, Jennifer A. Pietenpol, Philip S. Crooke, and Gieri Simonett.

I thank my collaborators on my papers, Carl Rogers and Drs. Anne K. Kenworthy, Jennifer A. Pietenpol, Shizhen Emily Wang, Carlos L. Arteaga, Christopher Barbieri, Erik M. Boczko, and Emmanuele DiBenedetto. Also I am indebted to the anonymous referees who greatly helped to improve my publications. My work has been supported by the NCI Integrative Cancer Biology Program (U54–CA113007) and the Vanderbilt Integrative Cancer Biology Center (VICBC) and I am grateful for that. Special thanks go to Drs. Vito Quaranta and Lourdes Estrada. I thank the College of Arts and Science at Vanderbilt University for a Summer Research Award in 2003 and a Travel Award in 2005. The Biomathematics Study Group at Vanderbilt University has generously supported my travels to important conferences in Scotland and Poland. Its director, Dr. Louis J. DeFelice is a wonderful mentor and friend. The office staff at the Mathematics Department as well as the librarians at the Science and Engineering library were always friendly and helpful and I am much indebted to them.

For helpful and encouraging discussions at several stages of this project I would like to thank Drs. Akram Aldroubi, Daphne Manoussaki and, again, Louis J. DeFelice, Erik M. Boczko and Gieri Simonett.

My fellow–students and friends have made my time at Vanderbilt University a

wonderful experience. I want to thank Matt Calef, Vladimir Chaynikov and Drs. Yuliya Babenko, Mihaela Bazalakova, Ana Carneiro, Sergey Borodachov, Dan Guralnik, Marcin Kozik, Ashot Minasyan, Aleksey Muranov, and Maxim Yattselev. I'm glad I've met you all and God bless you wherever you go. My family, although far away in Germany, Bulgaria and Switzerland, has been a continuous source of strength and inspiration. I want to thank all of them for their love and care. Finally I thank my girlfriend, Dr. Yuqiang Wei.

TABLE OF CONTENTS

LIST OF FIGURES

CHAPTER I

INTRODUCTION

Chapters II–IV of this thesis consist of adapted versions of the papers [29, 30] and [31], respectively, and can be read independently of each other. Finally, chapter V contains an analysis of two age–structured models from population dynamics.

In the work presented in chapter II, we investigated the diffusional motility of p53, a key tumor suppressor protein, in living cells using fluorescence recovery after photobleaching (FRAP). It is of great interest to understand the mechanisms by which proteins move in cells or membranes. Different photophysical methods have been developed over the past 30 years which allow researchers to study the mobility properties of membranous, cytoplasmic and nuclear proteins as well as other biomolecules or tracer particles. Commonly, a fluorescently labeled version of the protein of interest is constructed and transfected into suitable cells. In the case of FRAP, a non–equilibrium situation is created by applying a strong bleaching laser beam. The recovery of fluorescence due to movement of unbleached molecules is recorded and analyzed. This is where mathematical models enter the game as they are used to analyze and interpret the experimental data. In most cases, the first choice for a model is a partial differential equation that describes diffusion, driven by standard Brownian motion. If this first (simple) model turns out to be inadequate to describe observed experimental data, a second (more elaborate) model has to be considered, which can, for example, be a reaction–diffusion equation. In the case of p53, we found that diffusion of p53–GFP within the cell nucleus is well described by a mathematical model for diffusion of particles that bind temporarily to a spatially homogeneous immobile structure [30]. On the other hand, the inert protein GFP was found to diffuse freely and therefore provided a negative control. In the course of the analysis of our

experimental data we used a new statistical method to establish the significance of a parameter in a family of nested models. The data indicate that p53 undergoes nonspecific DNA binding (characterized by short residence times in the bound state) in unstressed cells. We also found evidence that p53–GFP is present in oligomers, in agreement with other biological data for p53.

The work that forms chapter III is likewise rooted in biophysics. An open problem is to understand how DNA–binding proteins (such as p53) find their specific target sequences in the genome. For example, one mechanism proposed in the literature is that of *crawling*, where a protein stays in contact with the fiber as it moves along the fiber. In contrast, the protein can also use *hopping*, where periods of association and disassociation interchange. In either case, the linear mass density profile of the fiber is expected to change in space and time. The goal of single molecule studies becomes to measure that density profile. In fact, this is precisely the objective of seismology, where the mathematics of inverse problems have been employed with success. Commonly, waves are sent into an elastic medium and responses are recorded and analyzed. We argue in [29] that inverse problems in elastic media can be directly applied to biophysical problems of fiber–ligand association. An additional difficulty is created by the fact that DNA fibers in an experiment will be supported in a viscous fluid. On the one hand this creates a loss of energy due to friction, on the other hand random forces act on the vibrating string and create a noise–contaminated response. We demonstrate that robust algorithms exist to perform density reconstruction in the condensed phase.

In chapter IV we turn to mathematical modeling of cytostatic and cytotoxic effects of the anticancer drug lapatinib. Human tumor cells are characterized by the dysregulation of gene expression. Over– and/or underexpression of select genes make them susceptible to treatment with targeted anti–cancer drugs that typically cause more damage to tumor–derived cells than to healthy cells. One example for this strategy

is the growth factor receptor HER2 and the targeted drug lapatinib that inhibits the activity of HER2. Lapatinib acts by slowing the progression of cells through the cell cycle (this is called a *cytostatic* effect), rather than inducing cell death (this would be called a *cytotoxic* effect). The cytostatic action is, however, cell cycle specific. Cells are affected according to their position in the cell cycle. Our goal in [31] was to quantitatively separate cytostatic and cytotoxic effects of lapatinib. As was seen through a combination of *in vitro* experiments and mathematical modeling, lapatinib slows preferentially the progression of cells through G_1 phase, the phase of the cell cycle during which most of the volume growth occurs. The data also indicated a previously unreported cytotoxic effect after long periods of drug exposure. Moreover, we investigated the temporal dynamics of the drug action and found that a gradual onset of cytostatic effects describes the data much better than a sudden onset. Our mathematical model is fully continuous with respect to time and maturity (the position of a cell in its cell cycle) and contains only a small number of parameters. These parameters have a straightforward biological interpretation and can be determined by examining the control scenario of the experiment. The model can be applied to a variety of drugs that have cell cycle specific cytostatic and cytotoxic effects.

Finally, in chapter V we analyze mathematically two age–structured models of population dynamics. A characteristic of many growth processes is that as the number of individuals reaches a certain threshold, the population growth slows. The Gompertzian growth model has been widely applied to such populations. In the case of a tumor cell mass, cells can belong to two distinct subpopulations, namely those of proliferating versus nonproliferating cells. The two models considered in chapter V differ in their interpretation of the "age" variable. In the first model, which was already used in chapter IV, age is interpreted as *maturity*, that is the position of a cell in its cell cycle. Nonproliferating cells do not progress in their cell cycle anymore, however, they are counted towards the total population. The transition from the pro-

liferating to the nonproliferating class is modeled by a nonlinear term that depends on the total population. We show that for such a model, both species approach finite limits as time approaches infinity. In the second model, age is interpreted as *chronological age*, that is the time since the last mitotic event from which the cell originated. In contrast to the first model it is also possible that nonproliferating cells return to the proliferating class. For a linear model of the same structure (with transitions between proliferating and nonproliferating classes independent of the total population), Dyson, Villela–Bressan and Webb [19] proved the property of *asynchronous exponential growth*. Intuitively, one expects the age distributions to reach a limit shape and the total mass to grow to infinity or decay to zero. The rate at which this growth occurs is called the *Malthusian* or *intrinsic* growth parameter and is determined as the solution of a characteristic equation. The situation is different in the nonlinear model under consideration, where transition rates between proliferating and nonproliferating classes depend on the total population. Under a certain natural condition, namely that both 0 and ∞ are repelling in the total population space, we show that the nonlinear population dynamic model based on chronological age must have a nontrivial equilibrium solution.

We end this thesis with a short outlook on ongoing and future research in chapter VI.

CHAPTER II

THE P53 DNA BINDING ACTIVITY

II.1 Introduction

A valuable tool to probe the architecture of the cell nucleus is fluorescence recovery after photobleaching (FRAP), see [14, 33, 48] for reviews and section II.2 for a short description. FRAP studies have revealed that many proteins involved in nuclear processes are highly mobile, yet diffuse more slowly than non–reactive, inert proteins of comparable size (such as green fluorescent protein, GFP) *in vivo* [54, 55, 71]. Careful analysis has revealed that for some nuclear proteins, FRAP curves cannot be adequately described by models based on free diffusion alone [12]. It has been proposed that fluorescently labeled molecules bind transiently to a spatially homogeneous immobile structure (immobile on the time scale of the experiment). This behavior can be described by a mathematical model [12, 71, 76] based on a reaction–diffusion equation for a mobile and an immobile species that interact through first–order chemical reactions.

Analytical solutions for the reaction–diffusion model have been derived for both circular and rectangular bleach geometries [71, 76]. For the latter case, the model assumes that the spatial domain available for diffusion of the fluorescent molecule of interest is a rectangle with one of its sides identified with the interval $[0, \ell]$. The density of the fluorescent molecules is assumed to be independent of the longitudinal variable of the rectangle and thus is a function $u(x, t)$ of $x \in [0, \ell]$ and time t [76]. The mathematical model is based on a reaction–diffusion equation for the density $u(x, t)$ set in the interval $[0, \ell]$ for all times $t > 0$, starting from its initial datum u_0. At $x = 0$ and $x = \ell$ homogeneous Neumann boundary conditions are imposed, since the

fluorescent molecules do not leave the compartment. The parameters at play are the diffusion constant D, the binding rate k_1 to the immobile structure, and the release rate from it, k_2. The values $k_1 = k_2 = 0$ would correspond to absence of immobile binding structures and thus free diffusion for $u(x,t)$. The density of fluorescent molecules $u(x,t)$ is integrated over a subset of $[0,\ell]$, called region of interest (ROI), and generates a theoretical, time–dependent, fluorescence signal $F(t; D, k_1, k_2)$, depending upon the unknown diffusion parameters $\{D, k_1, k_2\}$. By fitting the theoretical function to the experimental data one obtains estimates for these parameters.

Motivated by the key role of p53 in cancer biology and its well–characterized biochemistry, we determined whether the diffusional mobility of p53 within the nucleus can be described by the reaction–diffusion model. The tumor suppressor p53 is the most commonly mutated gene in human cancers. In response to cell stress, such as oncogene activation or DNA damage, p53 can function as a sequence–specific DNA binding transcription factor. p53 activates the transcription of genes involved in the processes of cell cycle arrest, DNA repair, and apoptosis, thereby protecting the genome from mutations and the organism as a whole from tumor formation. Using confocal FRAP, we analyzed the diffusion of a GFP–tagged form of p53. We extended the reaction–diffusion model to allow for flexibility in choosing the initial data by distinguishing the region where the bleaching laser beam is concentrated from the initial distribution profile of fluorescent molecules. This permits one to take into account the diffusion of unbleached molecules into the bleach spot and the diffusion of bleached molecules out of the bleach spot during the application of the bleaching laser beam, factors that can otherwise lead to an erroneous estimation of diffusion constants from confocal FRAP measurements [82, 86]. In addition, we used a nested model approach to test the statistical significance of fitting the data using the reaction–diffusion model versus simple free diffusion.

II.2 Experimental Procedures

For a detailed description of the Materials and Methods we refer to [30]. Fluorescence recovery after photobleaching (FRAP) rests on the following fact. The ability of a molecule to absorb and re–emit fluorescence photons can be lost after a certain number of such events. This chemical reaction just described is known as *photobleaching* and makes technologies such as FRAP possible. Further details can be also found in [28].

To study the mobility properties of a certain protein it is necessary to construct a covalent fusion of the protein of interest with a fluorophore. An often used natural fluorophore is green fluorescent protein (GFP), a protein that was cloned from the Pacific jellyfish *Aequoria victoria* in 1992. Typically a DNA plasmid that encodes the protein of interest together with the GFP tag is transfected into suitable cells which will then start to express the protein combination. The resulting protein then has to be tested whether it still localizes and functions as the wild–type (wt) protein does. For instance, in the case of a transcription factor (such as p53) the GFP–fusion should localize to the cell nucleus and induce the transcription of the target genes of the wild–type protein.

A uniform pool of fluorescently labeled protein is excited with a laser beam and resulting light is observed and recorded. A strong pulse of the same laser is then applied to irreversibly bleach a portion of the protein in a well–defined spot, see Figure 1. After the bleaching process the unbleached protein molecules will diffuse into the dark spot, hence an increase in fluorescence can be measured. In our study [30] we transfected p53–GFP into H1299 lung cancer cells which do not express p53 of their own. The length of a nucleus was typically $\ell = 20\,\mu m$, whereas the width of the bleached strip was $r = 1.1\,\mu m$ (with notations as if Figure 1). The bleach time was $530\,ms$. Fitting the theoretical recovery functions to the experimental recovery curves was done with the MATLAB standard function `lsqcurvefit`.

II.3 Mathematical Modeling

II.3.1 Geometrical Setup

We will employ two mathematical models for the recovery process. The first is based on free diffusion of a single species and contains one parameter, the diffusion constant D [14]. The second accounts for temporary binding of fluorescent molecules to an immobile structure [12, 13, 71, 76]. It contains three parameters, the (free) diffusion constant D as well as rate constants for the binding and unbinding reaction, k_1 and k_2, respectively. We will extend these models by choosing a more flexible initial condition which allows to factor in the effects of diffusion in and out of the bleach spot during the bleach time.

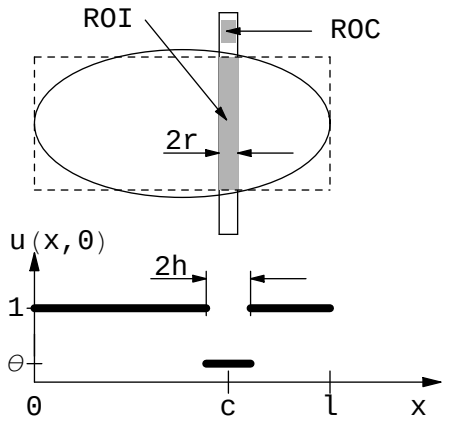

Figure 1: The geometrical setup of the FRAP experiment.

We assume a strip bleach geometry as shown in Figure 1. The compartment available to the fluorescent molecules (solid ellipse) is approximated by the dashed rectangle which in turn is projected onto its long side of length ℓ. The scanned bleach strip spans the full width of the rectangle and is indicated by the solid rectangle. It is centered at c and has half–width r. The region of interest (ROI) and the region of control (ROC) from which the signal respectively the background signal are collected are shaded gray. The initial datum to the recovery process is piecewise constant, with θ the bleach depth and h the half–width of the bleached region. The concentration

$u(x,t)$ of the fluorescent molecules is assumed to be independent of the longitudinal variable on the rectangle. The mathematical spatial domain thus becomes the interval $[0,\ell]$. Homogeneous Neumann conditions (zero flux condition) are imposed on $u(x,t)$ at $x = 0$ and ℓ. This means no exchange takes place across the boundary of the compartment (the nuclear membrane respectively the plasma membrane). The observation region is the interval centered at c and has length $2r$, modeled by an indicator function

$$I(x) = \begin{cases} 1 \text{ if } |x-c| \leq r \\ 0 \text{ otherwise} \end{cases}. \tag{1}$$

II.3.2 Free Diffusion

Let $u(x,t)$ denote the concentration of fluorescent molecules at position x at time t. The concentration is normalized to be one in the steady–state of the pre–bleach phase. The differential equation, boundary condition and initial condition for u are

$$\begin{aligned} \frac{\partial}{\partial t}u(x,t) &= D\frac{\partial^2}{\partial x^2}u(x,t), \\ \frac{\partial}{\partial x}u(0,t) &= \frac{\partial}{\partial x}u(\ell,t) = 0, \\ u(x,0) &= \begin{cases} 1 \text{ if } |x-c| > h \\ \theta \text{ if } |x-c| \leq h. \end{cases} \end{aligned} \tag{2}$$

Here c is the center of the bleached region, $2h$ is its width, and $0 \leq \theta < 1$ is the bleach depth (Figure 1). Notice the different meaning of r and h and that $r < h$ is possible. To the best of our knowledge in the current literature piecewise constant initial profiles are considered with $r = h$ and $\theta = 0$ only [12, 71, 76]. Thus in particular no distinction is made between initial datum, and observation region, at completion of the bleaching process.

A potential limitation of confocal FRAP measurements is that photobleaching is

accomplished by scanning the laser across the bleach region of interest, a process which takes a finite amount of time. As a result, during the bleach time unbleached molecules diffuse into the bleach spot, and bleached molecules diffuse out of it [10, 82, 86]. This results in an uncertainty about the initial datum of the recovery process. As remarked by Weiss in [86], the width of the bleached spot is larger and its boundaries are less sharp. This may cause an under–estimation of the diffusion constants by a factor of two to four.

The greater flexibility in the choice of the initial datum permits one to account for diffusion of fluorescent molecules into the bleach strip during the bleach time. The total mass of the initial datum from equation (2) should match its observed ultimate (asymptotic) recovery value,

$$\int_0^\ell u(x,0)\,\mathrm{d}x = \ell - 2h + 2h\theta = F_{\infty,obs}\ell.$$

Thus the width of the initial datum h must be chosen according to

$$h = \frac{\ell(1 - F_{\infty,obs})}{2(1-\theta)}.$$

The solution $u(x,t)$ of the system (2) is obtained by a standard Fourier series. Let

$$\lambda_0 = 0, \quad \lambda_j = \left(\frac{\pi j}{\ell}\right)^2,$$
$$\varphi_0(x) = \left(\frac{1}{\ell}\right)^{\frac{1}{2}}, \quad \varphi_j(x) = \left(\frac{2}{\ell}\right)^{\frac{1}{2}} \cos\frac{\pi j x}{\ell}, \quad j = 1, 2, \ldots$$

denote the eigenvalues and normalized eigenfunctions of the Laplace operator on $[0,\ell]$, with homogeneous Neumann boundary conditions. Then the solution to (2) is given

by the series

$$\begin{aligned} u(x,t) =& \sum_{j=0}^{\infty} \exp(-\lambda_j D t) \left(\int_0^{\ell} u(\xi,0)\varphi_j(\xi)\,\mathrm{d}\xi \right) \varphi_j(x) \\ =& \frac{\ell - 2h(1-\theta)}{\ell} + \frac{2(1-\theta)}{\pi} \sum_{j=1}^{\infty} \exp\left(-\frac{\pi^2 j^2 D t}{\ell^2} \right) \frac{1}{j} \\ & \times \left[\sin\frac{j\pi(c-h)}{\ell} - \sin\frac{j\pi(c+h)}{\ell} \right] \cos\frac{\pi j x}{\ell}. \end{aligned} \tag{3}$$

We multiply the series (3) by the intensity profile (1), integrate over $[0, \ell]$ and divide by $2r$ to obtain the theoretical recovery function

$$\begin{aligned} F_1(t;D) =& \frac{1}{2r} \int_{c-r}^{c+r} u(x,t)\,\mathrm{d}x \\ =& \frac{\ell - 2h(1-\theta)}{\ell} + \frac{\ell(1-\theta)}{r\pi^2} \\ & \times \sum_{j=1}^{\infty} \exp\left(-\frac{\pi^2 j^2 D t}{\ell^2} \right) \frac{1}{j^2} \left[\sin\frac{j\pi(c-h)}{\ell} - \sin\frac{j\pi(c+h)}{\ell} \right] \\ & \times \left[\sin\frac{j\pi(c+r)}{\ell} - \sin\frac{j\pi(c-r)}{\ell} \right]. \end{aligned} \tag{4}$$

From this we compute the asymptotic level of recovery as

$$F_{1,\infty} \stackrel{def}{=} \lim_{t\to\infty} F(t;D) = 1 - \frac{2h(1-\theta)}{\ell} < 1. \tag{5}$$

The parameter D is recovered by fitting $F(t;D)$ to the experimental data $F_{\mathrm{data}}(t_i)$, $i = 1, 2, \ldots, n$ at the discrete time points t_i.

II.3.3 Reaction–Diffusion Model

Suppose that fluorescent molecules are divided into mobile and immobile species, denoted by $u(x,t)$ and $v(x,t)$, respectively. It is assumed that the diffusion region contains a spatially homogeneous immobile structure, consisting of potential binding sites, to which fluorescent molecules can bind at rate k_1 and can be released from at

rate k_2. It is also assumed that the spatially homogeneous immobile structure always contains enough free binding sites so that saturation does not occur [71]. The three parameter model is given by

$$\begin{aligned}
\frac{\partial}{\partial t}u(x,t) &= D\frac{\partial^2}{\partial x^2}u(x,t) - k_1 u(x,t) + k_2 v(x,t),\\
\frac{\partial}{\partial t}v(x,t) &= k_1 u(x,t) - k_2 v(x,t),\\
\frac{\partial}{\partial x}u(0,t) &= \frac{\partial}{\partial x}u(\ell,t) = 0,\\
u(x,0) &= \frac{k_2}{k_1+k_2}\begin{cases} 1 & \text{if } |x-c| > h \\ \theta & \text{if } |x-c| \le h \end{cases},\\
v(x,0) &= \frac{k_1}{k_1+k_2}\begin{cases} 1 & \text{if } |x-c| > h \\ \theta & \text{if } |x-c| \le h \end{cases}
\end{aligned} \tag{6}$$

where c, h and θ are as in figure 1. The choice of the initial distribution is based on the assumption that an equilibrium between bound and unbound molecules has been achieved before the bleaching process, i.e. u and v are in steady state [12]. If $k_1 = 0$, then $v(x,0) = 0$ and the model reduces to the diffusion model (2). In this sense the one–parameter free diffusion model (2) is "nested" in the three–parameter reaction–diffusion model (6). This fact will be exploited in II.3.5 to discuss the statistical significance of the parameter k_1.

A solution to the model (6) is obtained by Fourier–Laplace transform techniques. With eigenfunctions of the Laplace operator φ_j as in II.3.2 we make the ansatz

$$u(x,t) = \sum_{j=0}^{\infty} u_j(t)\varphi_j(x), \qquad v(x,t) = \sum_{j=0}^{\infty} v_j(t)\varphi_j(x), \tag{7}$$

where $u_j(t), v_j(t)$ are to be determined from (6), with initial conditions

$$u_j(0) = \int_0^\ell u(x,0)\varphi_j(x)\,\mathrm{d}x, \qquad v_j(0) = \int_0^\ell v(x,0)\varphi_j(x)\,\mathrm{d}x.$$

The Laplace transform of $u_j(\cdot)$ is

$$\bar{u}_j(s) = \int_0^\infty e^{-st} u_j(t)\,\mathrm{d}t.$$

We insert the series (7) into the first two equations of (6), multiply by $\varphi_i(x)$ for a fixed index i, integrate over $[0,\ell]$ and take the Laplace transform of the resulting term. This gives

$$\begin{aligned} s\bar{u}_j(s) - u_j(0) &= -\left(\frac{j\pi}{\ell}\right)^2 D\bar{u}_j(s) - k_1\bar{u}_j(s) + k_2\bar{v}_j(s), \\ s\bar{v}_j(s) - v_j(0) &= \ k_1\bar{u}_j(s) - k_2\bar{v}_j(s). \end{aligned}$$

We solve for $u_j(s)$ and $v_j(s)$ and obtain

$$\begin{aligned} \bar{u}_j(s) &= \frac{(s+k_2)u_j(0) + k_2 v_j(0)}{(s+(j\pi/\ell)^2 D + k_1)(s+k_2) - k_1k_2}, \\ \bar{v}_j(s) &= \frac{(s+(j\pi/\ell)^2 D + k_1)v_j(0) + k_1 u_j(0)}{(s+(j\pi/\ell)^2 D + k_1)(s+k_2) - k_1k_2}, \end{aligned} \tag{8}$$

provided the denominator of these fractions is non–zero. The solutions of the equation

$$(s+(j\pi/\ell)^2 D + k_1)(s+k_2) - k_1k_2 = 0$$

are

$$s_{1,2;j} = -\frac{(j\pi/\ell)^2 D + k_1 + k_2}{2} \pm \frac{\sqrt{((j\pi/\ell)^2 D + k_1 + k_2)^2 - 4k_2(j\pi/\ell)^2 D}}{2}.$$

After a partial fraction decomposition of the expression (8), the Laplace transform can be inverted to give

$$\begin{aligned} u_j(t) =& (s_{1;j} - s_{2;j})^{-1} \\ & \times \Big([u_j(0) s_{1;j} + k_2(u_j(0) + v_j(0))] e^{s_{1;j} t} \\ & - [u_j(0) s_{2;j} + k_2(u_j(0) + v_j(0))] e^{s_{2;j} t} \Big), \\ v_j(t) =& (s_{1;j} - s_{2;j})^{-1} \\ & \times \Big([v_j(0)(s_{1;j} + (j\pi/\ell)^2 D + k_1) + k_1 u_j(0)] e^{s_{1;j} t} \\ & - [v_j(0)(s_{2;j} + (j\pi/\ell)^2 D + k_1) + k_1 u_j(0)] e^{s_{2;j} t} \Big). \end{aligned} \tag{9}$$

Both species are fluorescent and contribute to the normalized signal

$$\begin{aligned} F_2(t; D, k_1, k_2) &= \frac{1}{2r} \int_0^\ell [u(x,t) + v(x,t)] I(x) \, \mathrm{d}x \\ &= \frac{1}{2r} \int_{c-r}^{c+r} [u(x,t) + v(x,t)] \, \mathrm{d}x. \end{aligned} \tag{10}$$

To summarize, the theoretical recovery function is computed by first inserting the $u_j(\cdot)$ and $v_j(\cdot)$ computed in equation (9), into the expressions (7), and then by inserting the resulting $u(x,t)$ and $v(x,t)$ into (10). Since $s_{1;0} = 0$ and all other $s_{1,2;k}$ are negative, we compute the ultimate (asymptotic) level of recovery as

$$F_{2,\infty} \stackrel{def}{=} \lim_{t \to \infty} F_2(t; D, k_1, k_2) = 1 - \frac{2h(1-\theta)}{\ell}$$

which is the same as that in equation (5) for the free diffusion model. Observe further that in case $k_1 = 0$ we have $v_j(t) = 0$ and consequently for all k_2, $\tilde{k}_2$

$$F_2(t; D, 0, k_2) = F_2(t; D, 0, \tilde{k}_2) = F_1(t; D). \tag{11}$$

This implies that the level sets of the cost functional J from equation (13) in the plane $\{k_1 = 0\}$ are the lines $\{D = const\}$.

II.3.4 Potential Immobile Fraction

In our experiments we used two strategies to test for an immobile fraction. Before any bleaching the normalized fluorescence intensity is $F_0 = 1$. Assume that the compartment $[0, \ell]$ contains mobile and fully immobile (at the timescale of the experiment) fluorescent particles, their fractions being β and $1-\beta$, respectively. Suppose now that an interval of length $2h$ is completely depleted of fluorescent molecules. The recovery is due solely to the mobile fraction, therefore the level of recovery after a sufficiently long time will be, assuming conservation of mass

$$F_1 = (1 - \beta)\frac{\ell - 2h}{\ell}.$$

If the same region is now bleached again, only mobile particles will be destroyed. The second recovery will reach a level of

$$F_2 = (1 - \beta)\left(\frac{\ell - 2h}{\ell}\right)^2.$$

Hence, we have

$$1 - \beta = \frac{F_1^2}{F_2}. \tag{12}$$

In a second test, a region disjoint to the bleach region will be observed, in addition to the bleach region. The fluorescence recovery level in the unbleached region will be

$$F_1' = \beta + (1 - \beta)\frac{\ell - 2h}{\ell},$$

since the immobile molecules were not affected. It follows that

$$\beta = F_1' - F_1.$$

Notice that the actual size $2h$ of the bleached region in these experiments does not matter.

II.3.5 Determination of Parameters and Model Discrimination

For both models we derived theoretical recovery functions $F_l(t;q)$, $l = 1, 2$ by integrating the solution of the initial value problem weighted with the intensity profile. Denote by $q = (q_1, \ldots, q_p)$ the parameter of F_l (where $p = 1$ or $p = 3$). Given are the data points $(t_i, F_{data}(t_i))$, $i = 1, \ldots, n$. We assume the existence of a "true" parameter which, by definition, is a q^* such that

$$F_{data}(t_i) = F(t_i; q^*) + \varepsilon_i,$$

where the ε_i are independent, identically distributed random variables with mean $\mathsf{E}(\varepsilon_i) = 0$ and variance $Var(\varepsilon_i) = \sigma^2 < \infty$. An estimate for q^* is obtained by a least–square fit of $F(t;q)$ to the experimental data. That is, we minimize the cost functional

$$J(q) = \sum_{i=1}^{n} (F(t_i;q) - F_{data}(t_i))^2 \to \min_{q \in \mathcal{Q}_{ad}}, \tag{13}$$

where n is the number of data points making up the recovery part of the experiment and $\mathcal{Q}_{ad}$ denotes the set of admissible parameters. The set $\mathcal{Q}_{ad}$ can be chosen to be compact. Since the functional J is continuous with respect to q, the existence of a minimizer is guaranteed, denote any such minimizer by $\hat{q}$.

We now discuss the statistical test for the significance of the parameter k_1 proposed by Banks and Fitzpatrick in [5] applied to our situation. Choose the admissible

parameter set $\mathcal{Q}_{ad}$ such that it is compact and that the true parameter lies in its interior. Let

$$\mathcal{Q}_0 = \{(D, k_1, k_2) \in \mathcal{Q}_{ad} \,:\, k_1 = 0\}$$

be the restricted parameter set. We want to test the null–hypothesis $H_0 : q^* \in \mathcal{Q}_0$. Indeed, as we have seen, fixing the binding rate constant $k_1 = 0$ in equations (6) reduces the model to the simple diffusion model (2). Following [5], we calculate the statistic

$$U = \frac{J(\tilde{D}, 0, \cdot) - J(\hat{D}, \hat{k}_1, \hat{k}_2)}{J(\hat{D}, \hat{k}_1, \hat{k}_2)}. \tag{14}$$

Because of equation (11), it is possible to store the optimal value of the cost functional obtained from the one–parameter fit with the recovery function $F_1(\,\cdot\,; D)$ and use it in calculating the statistic from equation (14). Under certain assumptions on the noise process, the cost functional and the parameter space *and* if H_0 is true, it is proved in [5, Theorem 4.6] that the random variable U converges in distribution to a chi–square distributed random variable with 1 degree of freedom, as the number n of data points goes to infinity. We stress that the assumption on the noise process is only that it is a sequence of independent, identically distributed random variables with mean 0 and finite variance [5, Assumption (A1)].

II.4 Results

To ensure that the p53–GFP fusion protein was able to bind DNA and activate transcription similar to unmodified p53, we examined the ability of the p53–GFP fusion protein to upregulate p53 target genes. Ectopic (induced) expression of the p53–GFP fusion protein resulted in elevated levels of the p53 target gene products, p21 and mdm2 in a manner comparable to unmodified p53 protein. These data demonstrate that the p53–GFP fusion protein retains proper DNA binding and transcriptional activation capabilities. Furthermore, p53–GFP is correctly targeted to the nucleus of

H1299 cells.

We next determined if p53–GFP behaves as a mobile or immobile protein. To test for the presence of an immobile fraction (on the timescale of the experiment, $60\,s$), we performed confocal FRAP experiments on H1299 cells expressing p53–GFP. In the first series of experiments, we bleached a strip across the nucleus twice in succession [72]. If an immobile fraction is present it should be bleached completely the first time within the bleach strip but remain unaffected elsewhere. During the second bleach of the same strip only mobile molecules will be bleached.

We denote the asymptotic levels of recovery measured after the first and the second bleaching procedure by F_1 and F_2, respectively. Let β be the normalized volume of a possible immobile fraction. By the theoretical arguments II.3.4, equation (12) one has $\beta = 1 - F_1^2/F_2$. The experimental data however give $F_1^2/F_2 \approx 1$, which yields $\beta \approx 0$ and provides evidence against the presence of an immobile fraction (Figure 2 **A**). This experiment was performed three times with similar results. Thus we attribute the loss of fluorescence solely to the bleaching and do not assume the existence of an immobile p53–GFP fraction on the time scale of the experiment.

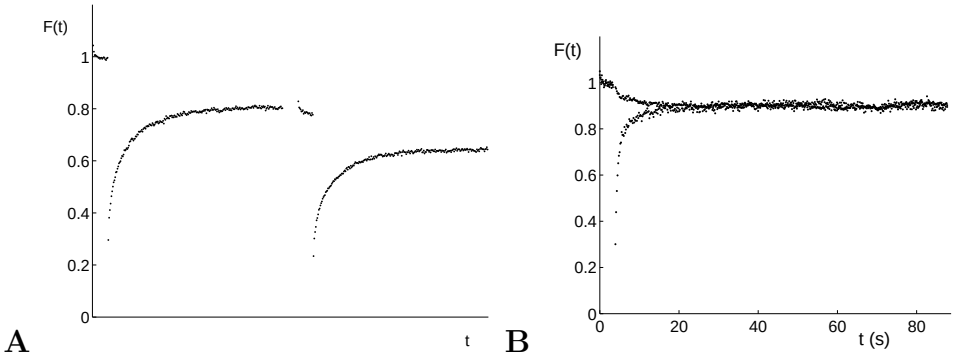

Figure 2: Tests for an immobile fraction.

A second test for an immobile fraction was conducted by bleaching a circular spot and measuring the asymptotic, normalized fluorescence at the bleach spot, and at another, unbleached circular region of equal radius, disjoint from the bleach spot, but

within the same domain of diffusion [53]. Let F_1 and F_1' be the respective ultimate recovery levels. Conservation of mass implies $\beta = F_1' - F_1$, whereas the data give $F_1' \approx F_1$ (Figure 2 **B**). Thus $\beta \approx 0$. These data are representative of four independent experiments.

Having determined that p53–GFP is fully mobile, we next assessed its diffusional mobility compared to that of GFP alone. Representative recovery curves obtained for p53–GFP and GFP in the nucleus are shown in Figure 3. We first tried to fit all curves with the theoretical recovery function $F_1(\,\cdot\,; D)$ from equation (4). However, apart from a few exceptional cases, the one parameter diffusion model was not able to explain the experimental data satisfactorily (Figure 3 **A**). Notice that the residuals of the optimal fit with the one parameter model in Figure 3 **A** are bimodal. We took this as reason to reject the one parameter diffusion model for p53–GFP.

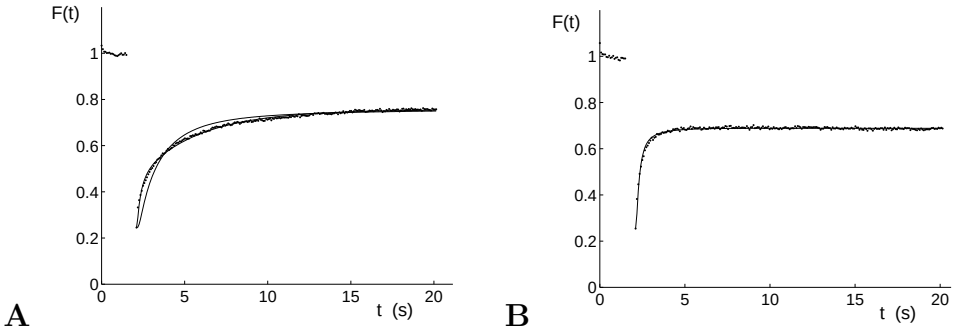

Figure 3: Representative fluorescence recovery curves for p53–GFP **(A)** and GFP **(B)**.

We then proceeded to fit the theoretical recovery function $F_2(\cdot; D, k_1, k_2)$, obtained from the three parameter model, equation (10), to the p53–GFP recovery curves. The diffusion constant of p53–GFP was estimated to be $D_{\text{p53–GFP}} = 15.4\,\mu m^2 s^{-1}$, significantly slower than that of GFP alone, which was found to be $D_{\text{GFP}} = 41.6\,\mu m^2 s^{-1}$. For GFP, on the other hand, in 7 out of 10 cases the one parameter model provided an acceptable fit of the experimental data, see Figure 3 **B** . Therefore we accept the hy-

pothesis that GFP is freely diffusing inside the cells. The experimentally determined mean parameter values for both p53–GFP and GFP are given in table II.1.

The diffusion constant obtained for GFP in the nucleus is in close agreement with values published in the literature, e.g. $D = 43 \pm 11\,\mu m^2 s^{-1}$ [89], $D = 58 \pm 9\,\mu m^2 s^{-1}$ [32] (although smaller values around $15\,\mu m^2 s^{-1}$ have also been reported, [71] and references therein).

The values of k_1 and k_2 obtained for p53–GFP using the reaction–diffusion model are suggestive of weak, non–specific binding [71], see section II.5.1 for more explanation of this terminology. In order to further test the contribution of specific DNA binding events to the apparent diffusion of p53–GFP, we performed FRAP experiments using tumor–derived p53 mutants that are deficient in sequence–specific DNA binding activity, R175H and R273H (arginine → histidine). Like p53–GFP, both p53 R175H–GFP and p53 R273H–GFP were targeted to the nucleus (data not shown). Approximately 40 FRAP experiments were carried out on each mutant protein, using the same experimental setup as for the wild type p53–GFP. For both mutants, the one parameter model was insufficient to fit the recovery curves, while the three parameter model provided an excellent fit. Significantly, the parameters of the three parameter fit were identical within error for those obtained for the sequence–specific DNA–binding mutants and the wild type p53 fusion protein. This further substantiates the notion that specific DNA binding does not contribute significantly to the slowed diffusion of p53–GFP compared to GFP.

Table II.1: The mean parameter values together with their standard deviations are shown.

protein	$D\,(\mu m^2 s^{-1})$	$k_1\,(s^{-1})$	$k_2\,(s^{-1})$
GFP	41.6 ± 13.6	–	–
p53–GFP	15.4 ± 5.6	0.31 ± 0.22	0.40 ± 0.13
R175H–GFP	17.9 ± 8.6	0.41 ± 0.30	0.41 ± 0.13
R273H–GFP	17.6 ± 8.2	0.39 ± 0.22	0.34 ± 0.12

II.5 Discussion and Conclusion

We have examined the nuclear diffusional mobility of p53–GFP using confocal FRAP. We show that p53–GFP is fully mobile, but exhibits slowed diffusion compared to GFP alone. We find that a free diffusion model is sufficient to explain the diffusional mobility of GFP in the nucleus. In contrast, p53–GFP exhibited more complex behavior consistent with a reaction–diffusion model, in which free diffusion is coupled with binding and release from an immobile structure. The lack of a difference between the diffusion properties of wild–type and the tumor–derived mutant p53 proteins suggests that under steady–state conditions the protein binds DNA in a sequence–independent manner. These data are consistent with a model that under steady state conditions, p53 is latent and continuously scans DNA, requiring activation for sequence–specific DNA binding.

Our data provide evidence against the existence an immobile fraction for p53–GFP. Immobile fractions have been suggested as a way of explaining the discrepancy between the observed, experimental partial recovery, versus the corresponding theoretical full recovery of fluorescent molecules.

II.5.1 The Mass of the Diffusing p53–GFP particle

The free diffusion constant for p53–GFP obtained from the reaction–diffusion model suggests that p53–GFP diffuses as an oligomer rather than a monomer. The free diffusion constants D_1 and D_2 of two spherical proteins of molecular weights m_1 and m_2 are linked by the formula

$$\frac{D_1}{D_2} = \left(\frac{m_2}{m_1}\right)^{\frac{1}{3}}. \tag{15}$$

Formula (15) is based on the assumption that the mass of a particle is proportional to the third power of its radius. Further, the diffusion constant is inversely proportional to the radius, according to the Einstein–Stokes formula [20]. The mass of GFP has

been reported to be $m_{\mathrm{GFP}} = 27\,kg/mole$ [87]. We estimate the mass of a single p53–GFP molecule to be $53+27 = 80\,kg/mole$. Using the averages $D_{\mathrm{p53–GFP}} = 15\,\mu m^2 s^{-1}$ and $D_{\mathrm{GFP}} = 40\,\mu m^2 s^{-1}$ in formula (15) one can estimate the mass of the diffusing p53–GFP particles to be

$$m_{\mathrm{p53–GFP}} = m_{\mathrm{GFP}} \left(\frac{D_{\mathrm{GFP}}}{D_{\mathrm{p53–GFP}}} \right)^3 > 500\,kg/mole.$$

This mass suggests that p53–GFP is present in an oligomerized form in the cell nucleus, that is, several individual p53–GFP molecules combine to form a larger particle. This estimate is robust qualitatively, in the sense that even assuming a smaller diffusion constant for GFP, say $D_{\mathrm{GFP}} = 30\,\mu m^2 s^{-1}$ would still give a mass $m_{\mathrm{p53–GFP}} > 200\,kg/mole$, again indicating the presence of an oligomerized form. We want to stress however, that this can serve only as a plausibility argument, since no information is presently available about the shape of the p53–GFP construct. Nonetheless, our data are consistent with early studies showing the predominant form of native, immunopurified p53 is a tetramer and that these tetramers can bind directly to DNA [22]. Several studies have convincingly shown that oligomerization is important for regulation of p53 transcriptional and tumor suppressive activities [15].

It is well known that transcription factors bind non–specifically to DNA, in addition to tight binding to their promoter sites. The inverse k_2^{-1} is considered as the average lifetime of the bound state. In this sense, Sprague et al. [71, p. 3482] have termed release rate constants k_2 around $10\,s^{-1}$ as typical for non–specific DNA binding whereas values near $10^{-6}\,s^{-1}$ indicate specific binding. We are aware that our experimental system overexpresses p53–GFP to some degree. Nevertheless we take our value $k_2 = 0.4\,s^{-1}$ as a sign of non–specific DNA binding of unmodified p53. This conclusion is supported by our observation that the diffusional mobility of DNA binding mutants and wild type p53–GFP are identical within error (Table

II.1). For comparison, Sprague et al. [71] estimate a binding rate $k_1 = 500\, s^{-1}$ and a release rate $k_2 = 86.4\, s^{-1}$ for GFP–tagged glucocorticoid receptor (GFP–GR) to be $D = 9.2\, \mu m^2 s^{-1}$.

II.5.2 Statistical Analysis

A novel contribution of [30] is the statistical analysis of acceptance or rejection of a model, as opposed to a statistical test of accepting or rejecting a specific value of a parameter. It has already been observed that the free diffusion model can be obtained from the reaction–diffusion model for the choice of the parameter $k_1 = 0$. This is a particular case of a family of "nested" models, that is an ordered finite collections of models. Roughly speaking, models of this family are generated by a *preceding model* by the inclusion of further hypotheses and parameters, in such a way that the preceding model is a particular case of the *subsequent model*, for special choices of the parameters. For such families, Banks and Fitzpatrick [5] have introduced a statistical method to test the significance of the subsequent model with respect to the preceding one. Given a model how statistically significant is it to expand the model by introducing new mechanisms and parameters? The statistical method of [5] was applied to test the significance of the binding rate constants k_1. It was found that the diffusion of p53–GFP cannot be explained by the free diffusion alone ($k_1 = 0$). This method of model discrimination can be applied to any protein, nuclear or otherwise, that is suspected to undergo binding events, provided that the mathematical models in use are nested.

CHAPTER III

MOLECULAR SEISMOLOGY

III.1 Introduction

In many situations and applications it is of interest to understand the *dynamics* of interaction between a biopolymer fiber and a ligand, a particle that binds to the fiber. For instance one would like to understand how proteins move along and around DNA fibers and interact with the various sequence elements in space and time. Crystal structures of proteins bound to DNA have shown how certain classes of transcription factors physically recognize specific DNA sequences, but these data contain very few if any clues about the dynamical processes that led to the observed static associations. The suggestion has been made that DNA binding proteins do not undergo three dimensional diffusion in the nucleus, but rather that they engage in essentially one dimensional diffusion by hopping or crawling on, along or between the fibers, possibly biased toward the DNA by a potential [23, 26, 81]. How does a DNA binding protein acquire a target site? Do DNA binding proteins home in on their cis regulatory elements (CRE) like a docking space shuttle guided by a potential? Is it possible for a DNA binding protein to collide with a fiber and then corkscrew along the double helix like a monorail, riding either the major or the minor groove?

At the core of the approach that we are proposing lies an inverse problem. Many problems in experimental science are inverse problems of one sort or another, since it is often easy to measure the output of a system as a whole. If the output is uniquely determined by some internal property then it becomes possible to invert the known output to determine the internal property.

The classic example of this is exploration seismology, where the elastic medium

is the ground, and how it vibrates in response to a sound wave is used to determine its material properties and perhaps the presence of low density pockets of oil. Consequently, there is a large literature and significant interest in inverse problems involving elastic media.

Waves and vibrations have tremendous discriminatory power. This power has been exploited in many disciplines and applications, but surprisingly not in biophysical assays involving polymer association. This omission seems purely historical and not technical. In this chapter we report our work on an inverse problem to detect molecular association of single molecules, and describe an algorithm that could conceivably be used for what we shall refer to as *molecular seismology*.

As said above, it is currently of great interest to measure how proteins are binding to an individual DNA fiber in space and time. For this application the DNA can usefully and practically be conceptualized as an elastic fiber along whose length there exists a well defined density profile ρ. As a ligand interacts and becomes associated with a fiber, the density profile will change in space along the fiber and in time if the ligand moves along the fiber or disassociates. Knowledge of the function $\rho(x,t)$ should inform us about the dynamics of the association process between the ligand and the fiber.

The central idea of molecular seismology is to subject single, solvated fibers to oscillation. How the induced waves propagate and scatter can depend sensitively and robustly on the material properties of the elastic fiber. Conversely, it is possible to determine the material properties of an elastic fiber from a measured trace of its vibration in response to a known impulse. If one can induce and measure vibrations along a single DNA molecule, incubated with proteins, the dynamics of the density profile will reveal the associated motion of the proteins along the fiber.

There is strong theoretical and practical evidence to suggest that dsDNA fibers can be accurately modeled as elastic fibers. Bishop et al. [9] investigate propagation

of bend and shear waves through and elastic rod and conclude that the chemical structure of DNA supports elastic wave propagation.

Well posed problems posses unique solutions that change continuously as a function of the input. For deterministic, semi–infinite strings as well as finite strings, the reconstruction of material profiles from data have been shown to be well posed under mild smoothness assumptions on the profile of the material property. Several algorithms have been proposed in the literature. We have extended one of these to fit our needs and use it to examine a set of feasible problems. As DNA–protein interactions take place in the condensed phase, thermal fluctuations and viscosity become important and can confound and degrade the ability to measure vibrations. Very little is known theoretically. A contribution of [29] is to examine these effects.

III.2 Statement of the Inverse Problem

We consider the one dimensional non–homogeneous wave equation with damping as a model for the transverse oscillation of the centerline of a double–stranded dsDNA fiber immersed in an aqueous heat bath,

$$\varrho(x)u_{tt}(x,t) + \nu u_t(x,t) - Eu_{xx}(x,t) = F(x,t). \tag{16}$$

The variable x represents the distance along the centerline and takes values in a finite interval $[0,\ell]$. Here u represents the transverse displacement of the centerline. The mass density $\varrho > 0$ is assumed to be twice differentiable, see [74, section 3]. The optimal, or weakest, conditions under which inversion theorems can be proved appear to be unresolved. The friction coefficient ν and the tension E are assumed to be positive, known constants. The external force F can be either deterministic, stochastic or some combination of both. A large part of this investigation is devoted to demonstrating that density inversion is possible for signals from elastic fibers immersed in a frictive

heat bath.

Throughout the remainder of this chapter, the function $\varphi(t)$ will denote a boundary source. The function $\psi(t)$ will represent additional information corresponding to a measured response at a boundary point. The boundary data considered here are either of Dirichlet $u(0,t) := \varphi(t)$, or Neumann $u_x(0,t) := \varphi(t)$ type. The function φ is usually chosen to be an approximation of the Dirac δ–function, although it can be chosen quite arbitrarily, since by linearity of equation (16) any particular choice determines the response to an impulse $\delta(t)$, and this in turn determines the complete Neumann–to–Dirichlet map [36, section 8.1]. Given initial and boundary conditions and a density profile it is possible to solve the wave equation (16) and determine the function ψ, the complementary boundary value. The goal is to study the inversion of this parameter–to–solution map $\varrho \mapsto \psi$.

The dynamics of the wave equation can be considered with a variety of initial and boundary conditions. Historically, in exploration geology, shear waves are induced into a quiescent elastic medium at a boundary and the reflected response is measured at the same boundary, the surface of the earth.This setup, born of necessity, is in fact extremely powerful and robust. The setup where excitation source and measurement occur at the same boundary point is called a *reflection problem*. In contrast, if the excitation takes place at one boundary point and the measurement at an interior point (possibly the other boundary point) one speaks of a *transmission problem*.

Theoretical results concerning the identifiability of material properties are generally formulated for wave equations that have been transformed into travel time coordinates. With the wave speed

$$c(x) = \sqrt{\frac{E}{\varrho(x)}}$$

one defines the new space variable z using the transformation

$$z(x) = \int_0^x c^{-1}(\xi)\,\mathrm{d}\xi \tag{17}$$

and calls z the *travel time*. Since the density is assumed to be strictly positive, the travel time transformation (17) is injective. This transformation is extremely useful because it "straightens out" the characteristic curves, see for instance [11] and [74, Figure 1]. It also makes it possible to define the parameter–to–solution map as a map between suitable function spaces. In the absence of friction and external forcing, i.e. if $\nu = 0$ and $F = 0$ in (16), the wave equation is transformed into

$$\eta(z)u_{tt}(z,t) - (\eta(z)u_z(z,t))_z = 0, \tag{18}$$

where

$$\eta(z) = \sqrt{E\varrho(z)}$$

is called the *acoustic impedance*. For the case $u_z(0,t) = \delta(t)$, Symes [73, Theorem 2] proved that $\psi(t) = u(0,t)$ on $[0,2T]$ determines the impedance $\eta(z)$ on $z \in [0,T]$, provided $\eta \in H^1[0,T]$. In addition Symes characterized the range of the map $\eta \mapsto \psi$ and provided a Lipschitz estimate of the type

$$||\eta_1 - \eta_2||_{H^1[0,T]} \leq C||\psi_1 - \psi_2||_{H^1[0,2T]} \tag{19}$$

where the ψ_i are the responses corresponding to the impedances η_i. The inequality (19) is local, i.e. it holds for all η_2 in a ball centered at η_1. An estimate of the type (19) is important with regard to the numerical stability of inversion algorithms.

It was shown in [62] and [1] that for a semi–infinite string whose impedance is constant after a certain point, the transmission and reflection problems are equivalent for the case of the Neumann–to–Dirichlet map (i.e. where $u_z(0,\,\cdot\,)$ is prescribed and

$u(T, \cdot)$ is measured). For an impedance $\eta \in H^1[0, 2T]$ that is constant for $T \leq t \leq 2T$, Rakesh and Sacks [62, Theorem 1] showed that $\psi(t) = u(T, t)$ for $t \in [T, 3T]$ uniquely determines η. Rakesh [60, 61] also showed that impedance inversion from the Dirichlet–to–Neumann map is well posed for a transmission problem and characterized the range of the parameter–to–solution map. However, the proof of this result depends on the fact that the string is semi–infinite and continues past the point of measurement with constant impedance.

III.3 The Inversion Algorithm

Many algorithms have been proposed to solve inverse problems stemming from one dimensional wave equations similar to equation (16). We want to mention here the paper by Santosa and Schwetlick [65], where the related impedance inversion problem for equation (18) is studied. We have extended and implemented a variational method proposed by Tadi in [75]. We have chosen this approach because it is flexible with respect to the model, flexible with respect to the boundary data, works directly with signals measured in real time (as opposed to travel time), and is robust with respect to noise. The robustness in the face of noise is not limited simply to additive noise in the measurement, but the method is robust with respect to natural noise arising from a frictive heat bath and modeled directly in the equations governing the elastic media.

The principal idea is to write the density profile as a separable function of space and time, with a fixed spatial basis and time varying coefficient functions. The time dependent coefficient functions are allowed to evolve from an arbitrary initial state to some final equilibrium that presumably fits the true density. For a measurement ψ on $[0, T]$, we follow [75] and define a regularized, least squares type, cost functional

for a pair (u, ϱ) by

$$J(u, \varrho) = \frac{1}{2} \int_0^T (\psi(t) - u(0,t))^2 \, \mathrm{d}t + \frac{\alpha}{2} \int_0^T \int_0^\ell \varrho_t^2(x,t) \, \mathrm{d}x \, \mathrm{d}t. \tag{20}$$

The constant $\alpha > 0$ is a regularization parameter [21, 40] which will play the role of a numerical damping constant in the iterative algorithm. Notice that the regularization term goes to zero when the density profile becomes stationary in time. The Euler–Lagrange equations that result from the cost functional (20) describe the equations of motion for the time dependent coefficient functions and these equations form the basis for an iterative numerical algorithm. We will explain the details in the remainder of this section.

III.3.1 Formulation of the Variational Problem

We begin by considering the reflection problem with boundary conditions

$$u(x,0) = u_t(x,0) = 0, \quad u_x(0,t) = \varphi(t), \quad u(\ell,t) = 0,$$

where, as stated before, the measurement takes place at the same point as the excitation

$$\psi(t) = u(0,t).$$

Define the set of admissible functions

$$\mathcal{D} = \{(u, \varrho) \in C^2([0,\ell] \times [0,T]) \times C^1([0,\ell] \times [0,T]) \, : \, \varrho > 0, \, u \text{ satisfies (16) } \}.$$

Let

$$G(x,t,u,\varrho) = \varrho(x,t) u_{tt}(x,t) + \nu u_t(x,t) - E u_{xx}(x,t) - F(x,t).$$

The cost functional J is constrained to the level set

$$G(x,t,u,\varrho)=0.$$

The augmented Lagrangian J^* becomes

$$J^*(u,\varrho,\lambda)=\frac{1}{2}\int_0^T(u(0,t)-\psi(t))^2\,\mathrm{d}t+\int_0^T\int_0^\ell\left[\frac{\alpha}{2}\varrho_t^2+\lambda G(x,t,u,\varrho)\right]\,\mathrm{d}x\,\mathrm{d}t,$$

where $\lambda(x,t)$ is the Lagrange multiplier. If $(\tilde{u},\tilde{\varrho},\tilde{\lambda})$ is an admissible variation at (u,ϱ,λ) then the variation of the augmented cost functional J^* in this direction is

$$\begin{aligned}\delta J^*(u,\varrho,\lambda;\tilde{u},\tilde{\varrho},\tilde{\lambda})=&\int_0^T(u(0,t)-\psi(t))\tilde{u}(0,t)\,\mathrm{d}t\\&+\int_0^T\int_0^\ell[\alpha\varrho_t\tilde{\varrho}_t+(\varrho u_{tt}+\nu u_t-Eu_{xx}-F)\,\tilde{\lambda}\\&\qquad+\lambda(u_{tt}\tilde{\varrho}+\varrho\tilde{u}_{tt}+\nu\tilde{u}_t-E\tilde{u}_{xx})]\,\mathrm{d}x\,\mathrm{d}t.\end{aligned}$$

Performing integration by parts on all terms that contain $\tilde{\varrho}_t$, $\tilde{u}_{tt}$, and $\tilde{u}_{xx}$ gives

$$\begin{aligned}&\delta J^*(u,\varrho,\lambda;\tilde{u},\tilde{\varrho},\tilde{\lambda})\\&\quad=\int_0^T(u(0,t)-\psi(t))\tilde{u}(0,t)\,\mathrm{d}t+\alpha\int_0^\ell\left[[\varrho_t\tilde{\varrho}]_0^T-\int_0^T\varrho_{tt}\tilde{\varrho}\,\mathrm{d}t\right]\,\mathrm{d}x\\&\quad+\int_0^T\int_0^\ell[(\varrho u_{tt}+\nu u_t-Eu_{xx}-F)\tilde{\lambda}+\lambda u_{tt}\tilde{\varrho}\,]\,\mathrm{d}x\,\mathrm{d}t\\&\quad+\int_0^\ell\left[[\lambda\varrho\tilde{u}_t-(\lambda\varrho)_t\tilde{u}+\nu\lambda\tilde{u}]_0^T+\int_0^T[(\lambda\varrho)_{tt}-\nu\lambda_t\,]\tilde{u}\,\mathrm{d}t\right]\,\mathrm{d}x\\&\quad-E\int_0^T\left[[\lambda\tilde{u}_x-\lambda_x\tilde{u}]_0^\ell+\int_0^\ell\lambda_{xx}\tilde{u}\,\mathrm{d}x\right]\,\mathrm{d}t.\end{aligned}$$

The boundary conditions on u require that we add variations $\tilde{u}$ which respect these, i.e.

$$\tilde{u}(x,0)=0,\quad\tilde{u}_t(x,0)=0,$$

$$\tilde{u}_x(0,t)=0,\quad\tilde{u}(\ell,t)=0.$$

This renders some of the boundary terms in the equation for δJ^* zero. We impose final conditions on the Lagrange multiplier

$$\lambda(x,T) = 0, \tag{21}$$

$$\frac{\partial}{\partial t}\left(\lambda(x,t)\varrho(x,t)\right)\Big|_{t=T} = \lambda_t(x,T)\varrho(x,T) + \lambda(x,T)\varrho_t(x,T) = 0. \tag{22}$$

Because of condition (21), condition (22) only implies that

$$\lambda_t(x,T) = 0$$

is necessary. In addition, λ must satisfy the spatial boundary condition

$$\lambda(\ell,t) = 0.$$

The boundary term containing ϱ must vanish,

$$\varrho_t(x,0)\tilde{\varrho}(x,0) = \varrho_t(x,T)\tilde{\varrho}(x,T) = 0.$$

This can only be achieved by requiring

$$\varrho_t(x,0) = \varrho_t(x,T) = 0,$$

since the alternative, imposing an initial respectively a final condition on ϱ itself is not sensible. We obtain the following necessary condition for a critical point of the augmented cost functional J^*

$$\int_0^T \int_0^\ell \Big\{ \Big[\left(-\alpha\varrho_{tt} + \lambda u_{tt}\right)\tilde{\varrho} + \left(\varrho u_{tt} + \nu u_t - E u_{xx} - F\right)\tilde{\lambda} + \left((\lambda\varrho)_{tt} - \nu\lambda_t - E\lambda_{xx}\right)\tilde{u} \Big] \,\mathrm{d}x \\ + \left(u(0,t) - \psi(t) - E\lambda_x(0,t)\right)\tilde{u}(0,t) \Big\} \,\mathrm{d}t = 0,$$

for all admissible variations. With the help of the Lagrange lemma [78] we obtain the following partial differential equations as necessary conditions to a minimizer

$$\begin{aligned} \varrho u_{tt} + \nu u_t - E u_{xx} &= F, \\ (\lambda\varrho)_{tt} - \nu\lambda_t - E\lambda_{xx} &= 0, \\ -\alpha\varrho_{tt} + \lambda u_{tt} &= 0. \end{aligned} \tag{23}$$

together with the boundary condition

$$u(0,t) - \psi(t) = E\lambda_x(0,t). \tag{24}$$

These equations are supplemented by the initial, final and boundary conditions.

To adapt the above strategy to the transmission problem (32) it is necessary to modify the cost functional to take into account the boundary conditions

$$J(u,\varrho) = \frac{1}{2}\int_0^T (\psi(t) - u(\ell,t))^2 \,\mathrm{d}t + \frac{\alpha}{2}\int_0^T \int_0^\ell \varrho_t^2(x,t)\,\mathrm{d}x\,\mathrm{d}t.$$

The same partial differential equations (23) are obtained. The backward adjoint equation has to be supplied with the boundary condition

$$\lambda_x(0,t) = 0, \quad E\lambda_x(\ell,t) - (\psi(t) - u(\ell,t)) = 0.$$

For the problem with homogeneous Dirichlet boundary conditions (33)–(34) the cost functional J becomes

$$J(u,\varrho) = \frac{1}{2}\int_0^T \Big((\psi_1(t) - u_x(0,t))^2 + (\psi_2(t) - u_x(\ell,t))\Big)^2 \,\mathrm{d}t + \frac{\alpha}{2}\int_0^T \int_0^\ell \varrho_t^2(x,t)\,\mathrm{d}x\,\mathrm{d}t.$$

The boundary conditions to the backward adjoint equation are derived

$$E\lambda(0,t) - (\psi_1(t) - u_x(0,t)) = 0, \quad -E\lambda(\ell,t) - (\psi_2(t) - u_x(\ell,t)) = 0.$$

For the inverse problem with homogeneous Neumann boundary conditions, the cost functional J becomes

$$J(u,\varrho) = \frac{1}{2}\int_0^T \left((\psi_1(t) - u(0,t))^2 + (\psi_2(t) - u(\ell,t))^2\right) \mathrm{d}t + \frac{\alpha}{2}\int_0^T \int_0^\ell \varrho_t^2(x,t)\,\mathrm{d}x\,\mathrm{d}t.$$

The boundary conditions to the backward adjoint equation are derived

$$-E\lambda_x(0,t) - (\psi_1(t) - u(0,t)) = 0, \quad E\lambda_x(\ell,t) - (\psi_2(t) - u(\ell,t)) = 0.$$

III.3.2 The Iterative Algorithm

We describe the iterative algorithm used to solve the Euler–Lagrange system that results for the inversion problem from reflection data for the case of the Neumann–to–Dirichlet map. The method of solution for the other cases is completely analogous.

First we argue that there exists a unique optimal solution. Let the true density $\varrho^* = \varrho^*(x)$ be given. Let u^* be the corresponding solution of the wave equation (16) with boundary conditions (30). Then clearly the second equation of (23) together with boundary condition (24) imply that the Lagrange multiplier vanishes identically. This in turn implies that $\varrho_{tt} = 0$, and with $\varrho_t(0,x) = 0$ it follows that ϱ is independent of time. In summary, the triple $(u^*, \varrho^*, \lambda^* \equiv 0)$ is the unique solution of the system of partial differential equations (23). This implies that the pair (u^*, ϱ^*) is a critical point of the regularized cost functional J from equation (20) constrained to the level set $\{G(u,\varrho) = 0\}$, with $J(u^*, \varrho^*) = 0$ as the critical value. Of course, since $\alpha > 0$, this is the global minimal value of J.

Suppose that an approximate density $\varrho^n = \varrho^n(x)$, $n \geq 1$ has already been calculated. During an iteration step this time–independent density is used to determine the solution u^n of the forward wave equation and the solution λ^n of the backward adjoint equation

$$\varrho^n(x)u^n_{tt}(x,t) + \nu u^n_t(x,t) - Eu^n_{xx}(x,t) = F,$$
$$\varrho^n(x)\lambda^n_{tt}(x,t) - \nu\lambda^n_t(x,t) - E\lambda^n_{xx}(x,t) = 0,$$

subject to the boundary condition

$$-(\psi(t) - u^n(\ell,t)) + E\lambda^n_x(\ell,t) = 0.$$

Using u^n and λ^n, the equation

$$\varrho_{tt}(x,t) = -\frac{1}{\alpha}\lambda^n(x,t)u^n_{tt}(x,t) \tag{25}$$

is integrated forward in time, with initial conditions $\varrho(0,x) = \varrho^n(x)$, $\varrho_t(0,x) = 0$. To ensure that the value of the cost functional is decreased, we have to switch the "direction" along which $\varrho(x,t)$ evolves, hence the minus sign in equation (25), [90]. The density is updated according to

$$\varrho^{n+1}(x) = \varrho^n(x) - \frac{1}{\alpha}\int_0^T \int_0^\tau \lambda^n(s,x)u^n_{tt}(s,x)\,\mathrm{d}s\,\mathrm{d}\tau.$$

III.4 The Frictive Heat Bath

A principal difference between the inverse problem in seismology and biology, apart from the scale, is the addition of a frictive heat bath. Intracellular biology happens in the condensed phase and the DNA fibers we wish to investigate are suspended in aqueous solution. The fiber is constantly hit by the molecules of the fluid which

act as a driving force. The effects of a heat bath are traditionally and elegantly incorporated into molecular models through the combination of viscous dissipation and random forcing.

We model viscous dissipation by adding $\nu u_t(x,t)$ on the left hand side of equation (16). We also add a random force $F(x,t) := \dot{W}(x,t)$ on the right hand side of equation (16). The notation $\dot{W}$ stands for *white noise*, the (distributional) derivative of the Brownian sheet W, see [83]. The number of molecules hitting a portion dx of the string during a time ds will be essentially independent of those hitting a different portion dy during a time dt. Thus we think of the external force F as of a stochastic process with expectations

$$\begin{aligned} \mathsf{E}[F(x,t)] &= 0, \\ \mathsf{E}[F(x,t)F(y,s)] &= \sigma^2 \delta(t-s)\delta(x-y). \end{aligned} \tag{26}$$

The solution of the stochastic wave equation is defined as a stochastic process that satisfies the weak (integral) form of the partial differential equation [83]. See also the papers by Belinskiy and Caithamer [6, 7].

As described in section III.3, the cost functional J can be utilized with equations that model a heat bath. We have utilized this approach to study density reconstruction from various boundary and initial conditions corresponding to potential experimental designs for manipulating dsDNA fibers in solution. We have identified two distinct and natural numerical approaches. In an approach denoted as *average over realizations* (AOR), a signal is recorded from the model with a realization of the random force F. The Euler–Lagrange equations (23) directly model this force, but while we have measured the system response $\psi(t)$, we do not have access to the particular realization of the random force. Thus, we perform the numerical reconstruction to convergence, with a random realization of the force that has the same parameter σ. The reconstruction procedure is performed m times, and results in m

reconstruction ϱ_i, from different realizations F_i of the random force. It is natural to consider the pointwise average of these

$$\bar{\varrho} = \frac{1}{m} \sum_{i=1}^{m} \varrho_i. \tag{27}$$

In a second approach denoted as *average over signals* (AOS) we take advantage of the fact that the average of the random force is zero. In this approach we average several recorded signals to produce

$$\bar{\psi} = \frac{1}{m} \sum_{i=1}^{m} \psi_i. \tag{28}$$

and apply the reconstruction algorithm with mean force equal to zero.

III.5 Results

A standard finite–difference leapfrog scheme was used for the numerical integration of all occurring wave equations [59]. Spatial discretization was accomplished using piecewise constant functions. The tension parameter was chosen $E = 1$. Computations were performed with MATLAB and the random force was implemented using the function `randn`.

We anticipate, at least initially that a single protein will be binding a DNA fiber. For this reason, and because it is imagined that signal to noise issues will pose the dominant experimental challenge, it is sufficient for us to confine ourselves to the consideration of a simple density profile. The behavior of the cost functional for a reflection problem, without intrinsic noise and damping, was thoroughly explored on a large variety of density profiles in [75]. Our focus is on alternative boundary conditions and reconstructibility in the condensed phase. In order to meaningfully compare the performance as a function of noise strength it is important to have a gold

standard density profile. Therefore, we confine our attention to the reconstructibility of the following smooth density profile

$$\varrho^*(x) = 1 + \exp\left(-\frac{(x-1/2)^2}{(1/5)^2}\right). \tag{29}$$

The natural starting density profile for the iterative algorithm is a constant density. In the AOR procedure it may be desirable to converge solutions from a variety of independent initial conditions, although we do not focus on this possibility here.

A finite width, smooth approximation of a delta pulse was used as excitation in the Neumann–to–Dirichlet transmission and reflection problems. As with most iterative algorithms, one must choose a heuristic stopping criterion. A reasonable criterion for terminating the iteration procedure is to consider the improvement of the cost functional

$$\mathcal{S}(n) = \frac{J(\varrho^n)}{J(\varrho^1)}.$$

Through preliminary reconstructions it was observed that the presence of damping did not prevent convergence but rather only slowed the rate of convergence. Values of $\mathcal{S}$ as a function of damping strength are reported in table III.1. Given the data in table III.1 and the theory described in [6, 7] it is reasonable to fix the damping parameter $\nu = 1$ in subsequent reconstructions and explore a range of noise strengths.

Table III.1: Normalized improvement of the cost functional $\mathcal{S}$ after 200 and 400 iterations for a reflection (R) and a transmission (T) problem.

ν	$\mathcal{S}_R(200)$	$\mathcal{S}_R(400)$	$\mathcal{S}_T(200)$	$\mathcal{S}_T(400)$
0	$1.23 \cdot 10^{-5}$	$1.47 \cdot 10^{-6}$	$1.53 \cdot 10^{-4}$	$2.24 \cdot 10^{-5}$
1	$2.2 \cdot 10^{-3}$	$1.18 \cdot 10^{-4}$	$2.96 \cdot 10^{-2}$	$9.11 \cdot 10^{-3}$
2	$3.23 \cdot 10^{-2}$	$1.08 \cdot 10^{-2}$	$5.7 \cdot 10^{-2}$	$3.9 \cdot 10^{-2}$

III.5.1 Reconstruction from Reflection

Suppose the source $\varphi(t)$ and the measurement $\psi(t)$ are placed at the same boundary point, 0, of the interval $[0, \ell]$. There are 4 choices of boundary conditions that give rise to a well–posed direct problem. Since the boundary condition at the far end does not influence the response up to the two–way travel time only two choices are relevant,

$$u_x(0,t) = \varphi(t), \qquad u(\ell,t) = 0, \quad \psi(t) = u(0,t), \qquad \text{and} \tag{30}$$

$$u(0,t) = \varphi(t), \qquad u(\ell,t) = 0, \quad \psi(t) = u_x(0,t). \tag{31}$$

The Neumann–to–Dirichlet boundary setup (30) proved to be the most robust in the sense that it produced the highest quality reconstructions with the fewest iterations, and the algorithm showed excellent convergence toward the true density, under all conditions of noise for both reconstruction strategies and with all density profiles. Reconstructions from signals with damping but without random forcing converge rapidly to the true density ϱ^*, as can be seen in Figure 4 **A**, where the 200th and 400th iterates are shown against the true density (29). An AOS reconstruction is shown in Figure 4 **B** in comparison with the true density. To obtain this picture 20 responses were averaged according to equation (28), with noise strength $\sigma^2 = 4$ (see equation (26)) and damping $\nu = 1$.

Forty reconstructions from a randomly forced ($\sigma^2 = 4$), damped string ($\nu = 1$), each using a different realization of the random force are shown in Figure 5 **A**. Their average according to equation (27) is shown in Figure 5 **B**.

In contrast, the Dirichlet–to–Neumann reflection problem (31) was more subtle and we were not able to converge reconstructions through the cost functional optimization using simple delta forcing. This generic forcing was not able to induce discrimination between the responses to constant and unimodal impedances as can

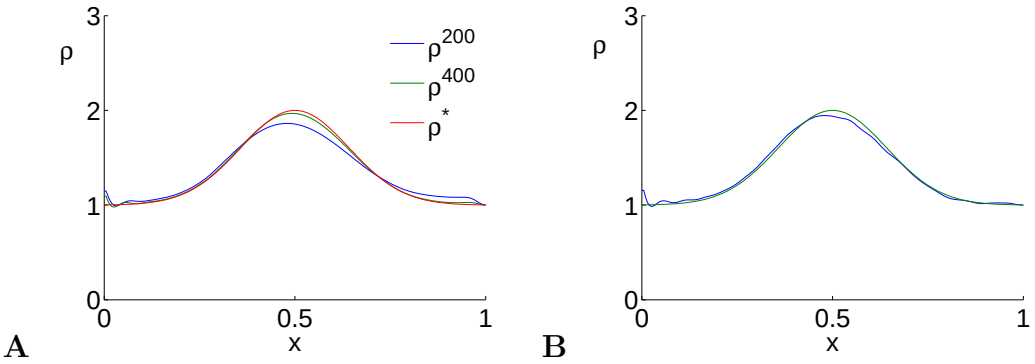

Figure 4: Results of the iterative reconstruction algorithm.

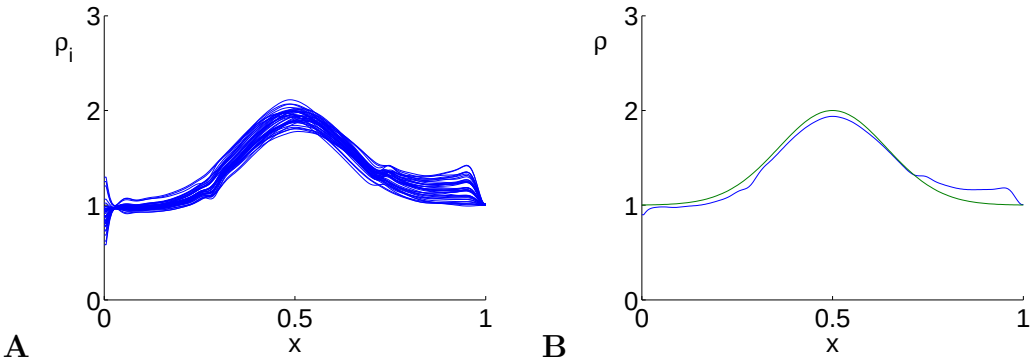

Figure 5: Results of the AOR reconstruction procedure.

be seen in Figure 6 **A, B**. Figure 6 **A** shows the Dirichlet responses $u(0,t)$ of a wave equation in impedance form (18) (without damping and external forcing) to a pulse $u_y(0,t) = \delta(t)$, where one string has constant impedance and the other string has an impedance similar to (29). One sees a clear separation of the responses. This has to be contrasted against Figure 6 **B**, where the Neumann responses $u_y(0,t)$ are shown, after the strings were excited by a pulse $u(0,t) = \delta(t)$. The failure of the cost functional optimization algorithm in this situation is purely numerical in the sense that theorems exist, as described in section III.2, that guarantee that the inverse problem has a unique solution. Furthermore, the algorithm of Santosa and Schwetlick [65], that is completely symmetric with respect to φ and ψ and consequently with respect to the two distinct boundary conditions, was able to exactly reconstruct the true

density profile from impulse forcing for an undamped, inhomogeneous wave equation in impedance form without random forcing. However, the algorithm of [65] failed when even the slightest damping and/or noise were introduced. There seems to be no analytical result comparable to that of [73] if damping is present. It is important to observe that the two algorithms are founded on completely different principles and that the algorithm of [65] determines the impedance directly from a single response through its behavior along a special characteristic line $y = t$. We were able to obtain convergent reconstructions for problem (31) with cost functional optimization using sinusoidal forcing (data not shown). In Figure 6 **C** we show the Neumann responses $u_y(0,t)$ of the same strings when they are subjected to sinusoidal forcing $u(0,t) = 8\sin(2\pi t)$. The obvious drawback is that in contrast to the generic impulse forcing, sinusoidal forcing requires a choice of frequency. Given that we know the true density in our theoretical experiments, it is straightforward to find such a frequency, but in an actual experiment this will be more difficult unless we can discover a systematic and natural solution to this problem.

III.5.2 Reconstruction from Transmission

If the source and receiver are placed at opposite ends of the fiber then four distinct well–posed problems result. Of these we focus on the Neumann–to–Dirichlet problem

$$u_x(0,t) = \varphi(t), \quad u_x(\ell,t) = 0, \quad \psi(t) = u(\ell,t). \tag{32}$$

The AOS procedure was relatively insensitive to noise in the transmission problem (32), just as in the reflection problem. In contrast, however, the AOR procedure produced not only more accurate results than the AOS procedure, but the accuracy improved with increasing noise strength, in sharp contrast to the behavior observed in the reflection problem. A partial understanding of this phenomena is provided

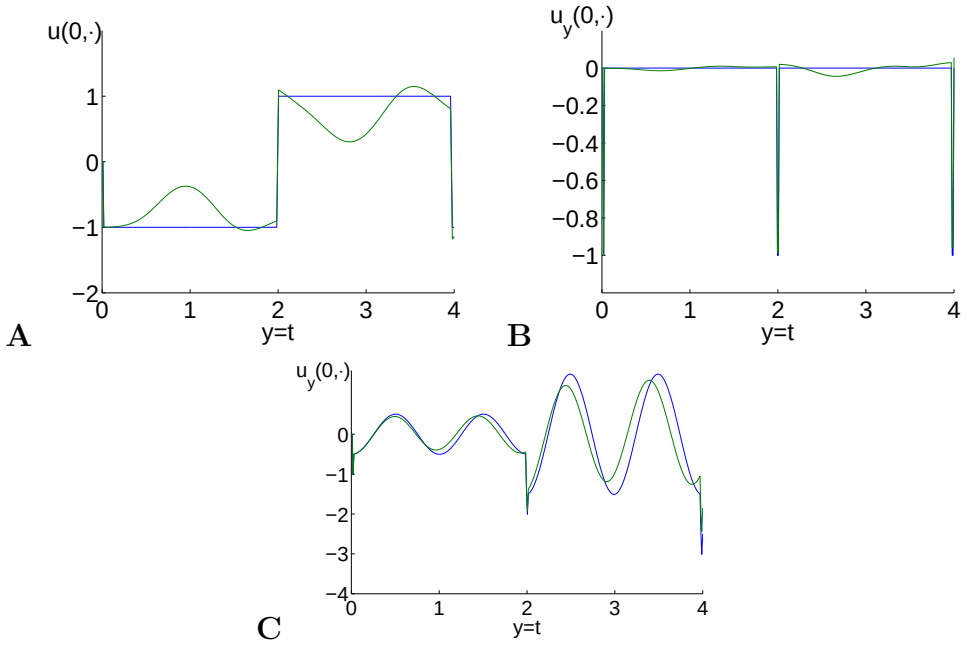

Figure 6: Different discriminative powers for Neumann–to–Dirichlet and Dirichlet–to–Neumann problems.

by observing and contrasting the individual reconstructions used to compute the AOR average. In the reflection problem it was observed that independent of the starting value of the constant density profile, the iterations generally approached the true density from below. While, in the transmission problem, the individual reconstructions, that differ in the particular realization of the random force, were far more uniformly distributed about the true density. In this way the noise appears to have allowed the iterations to approach the global minimizer from different directions on the cost surface.

III.5.3 Homogeneous Boundary Conditions

In both the transmission and reflection problems described above, the motion of the fiber was actuated at a boundary point. In this and the following section we consider two problems in which data are collected at the boundaries but the vibrations are

induced through initial data

$$u(x,0) = u_0(x), \quad u_t(x,0) = v_0(x). \tag{33}$$

The problems are homogeneous in the sense that the boundary conditions are the same at both ends of the fiber. Two measurements are taken, the complementary data at both ends. Thus in the Dirichlet case we have

$$\begin{aligned} u(0,t) = 0, \quad u(\ell,t) = 0, \\ \psi_1(t) = u_x(0,t), \quad \psi_2(t) = u_x(\ell,t). \end{aligned} \tag{34}$$

The homogeneous Neumann case

$$\begin{aligned} u_x(0,t) = 0, \quad u_x(\ell,t) = 0, \\ \psi_1(t) = u(0,t), \quad \psi_2(t) = u(\ell,t). \end{aligned}$$

behaved in a qualitative and quantitatively similar way and we omit these results.

III.6 Conclusions

We have demonstrated in [29] that robust density reconstruction from synthetic signals of an elastic fiber in a viscous heat bath is possible from at least four different boundary conditions. Based on the premise that some material profile along a single molecule of DNA will change as ligands associate with it, we have proposed an inverse problem to image this change in space and time. We have shown that both theoretically and numerically it is possible to invert density profiles from simple elastic models. Moreover we have shown that it is possible to do so from fibers immersed in a frictive heat bath in a natural way. Informed by known mathematical theorems, our numerical results, and the key technical developments in the field of nanofabrica-

tion and single molecule detection, we have proposed an experimental strategy with which it may be possible to record the signals required by our theory of molecular seismology. Preliminary experiments with DNA fibers suspended in solutions are under way in the laboratory of Dr. Charles Brau, Department of Physics and Astronomy, Vanderbilt University.

CHAPTER IV

CYTOSTATIC AND CYTOTOXIC ACTION OF A HER2 TYROSINE KINASE INHIBITOR

IV.1 Introduction

Molecule–targeted anti–cancer drugs have been developed as a result of our understanding of tumor cell and molecular biology. Compared to "traditional" cancer therapies, targeted drugs such as the tyrosine kinase inhibitors (TKIs) have higher specificity and relatively lower toxicity in selected patients with corresponding oncogene expression. Members of the type 1 receptor tyrosine kinase (RTK) family, which includes the epidermal growth factor receptor (EGFR), HER2 (ErbB2), HER3 and HER4 play a crucial role in growth and differentiation of both normal and malignant mammary epithelial cells [34, 63]. Binding of receptor–specific ligands to the ectodomain of EGFR, HER3 and HER4 results in the formation of receptor dimers and hetero–oligomers to which HER2 is recruited as the preferred heterodimerization partner [88]. HER2 gene amplification has been reported in approximately 20% of breast cancers, where it is associated with poor patient outcome [68]. Studies with HER2–overexpressing breast cancer cell lines and human tumors have shown constitutive phosphorylation of HER2 [2, 77]. Overexpression of HER2 is associated with transformation of mammary epithelial cells [50, 56] as well as shorter survival in patients with breast carcinoma [64, 68]. These findings make HER2 a rational therapeutic target in human breast cancer.

Lapatinib is a selective reversible inhibitor of both EGFR and HER2 tyrosine kinases. Lapatinib mimics ATP (adenosine triphosphate) and binds to the ATP site in the tyrosine kinase domain of HER2, resulting in blockade of the receptor's catalytic activity [69]. Preclinical data have shown that tumor cells overexpressing

EGFR or HER2 are growth inhibited by lapatinib both in vitro and in vivo [37, 42, 51]. In a study in which over 30 breast cancer cell lines were tested for their responses to lapatinib, concentration–dependent antiproliferative effects of lapatinib were seen in all cells but varied significantly between individual cell lines [42]. Response to lapatinib is significantly correlated with HER2 expression and its ability to inhibit the phosphorylation of HER2 and downstream effectors. In phase II clinical trials, treatment with lapatinib resulted in objective tumor responses in 28% of patients with HER2–positive advanced breast cancer [37]. Modeling the antiproliferative effects of this oncogene inhibitor using mathematical tools will lead to novel insights into the functioning features and mechanisms of the inhibitor. The model may also provide constructive clinical implications, such as the predictive effects of the inhibitor in first–line therapy in combination with chemotherapy.

In the study [31] we used MCF10A human mammary epithelial cells engineered to overexpress HER2 in order to determine the anti–tumor effects of lapatinib. Compared to control MCF10A cells that do not overexpress HER2, MCF10A/HER2 cells exhibit a gain–of–function phenotype including increased proliferation, as a result of oncogene overexpression [84]. Lapatinib inhibits the phosphorylation and function of HER2 in these cells and suppresses growth [84]. Quantitative models can separate the strengths of drug action on individual phases of the cell cycle. Previous molecular biological studies have shown that HER2 is associated with increases of both G_1–S–specific cyclins (cyclins D and E) and G_2–M–specific cyclin (cyclin A) [27, 43], which are crucial for G_1–S and G_2–M progression, respectively. Our objective in [31] was to use quantitative models to determine if HER2 inhibitors abolish the function on both phase transitions and how this contributes to cell cycle blockage.

Mathematical modeling has been applied extensively to study the growth kinetics of tumors, with and without treatment; for a small selection see [8, 24, 25, 38, 39, 46, 70, 80] and the references therein. These authors have focused on phenomena such

as decelerated growth, quiescence, homeostasis and chemotherapy scheduling. Most often, partial differential equation models have been used, with spatial position or age of cells as independent variables.

It has been recognized that, apart from killing cells outright, anticancer drugs can also act by delaying the progression through the cell cycle. Moreover, this blocking effect can be phase specific [49]. Transition through one phase of the cell cycle may be delayed while transition through another phase is unaffected. Mathematical modeling here provides the tool to test possible alternative scenarios against each other and to gain new insight. In a series of papers, Ubezio and collaborators used a mathematical modeling approach to investigate phase–specific cytotoxic and cytostatic effects of drugs such as cisplatin, melphalan and topotecan *in vitro* [44, 45, 49, 80]. The model of Ubezio et al. [49] uses discrete compartments for the maturity of cells and the time likewise proceeds in discrete steps. The model is difficult to handle as it relies on a large number of parameters that are not easily interpreted biologically. On the other hand, a continuous partial differential equation model has been used by Agur and coworkers [38] to theoretically predict the effect of periodic treatments with cycle–specific cytotoxic drugs.

IV.2 Experimental Procedures

For a detailed description of the Materials and Methods we refer to [31]. Briefly, MCF10A/HER2 (engineered to overexpress HER2) cells were grown on 6–well plates over a time course of 6 days. In addition to the control scenario, cells were treated with different concentrations (0.1, 0.5, 1 and 2 μM) of lapatinib that was added and left in the medium throughout. At certain time points (every 8 respectively 24 hours), the total cell number was counted and the cell cycle distribution was determined using flow cytometry. First, the DNA in each cell of a large population (say 10^4 cells) is tagged with the fluorescent marker propidium iodide. The flow cytometer then

determines from the strength of the fluorescence signal the DNA content in each cell and produces a histogram. Cells can then be grouped into compartments according to their DNA content ($n \mapsto \mathrm{G}_1$, $2n \mapsto \mathrm{G}_2/\mathrm{M}$); see also [80] for a detailed description. Recall that during the growth phases G_1 and G_2 the cell increases its volume while during the synthesis phase S the DNA is duplicated. Finally, during mitosis M, the DNA is split evenly among the resulting daughter cells.

The mathematical model was designed to quantify the cytostatic and cytotoxic effects of the drug on the basis of the population dynamics observed in the experiments. The model consists of a system of differential equations describing these dynamics over the 6 day time course (see section IV.3 for a detailed description). Cells are classified as proliferating or nonproliferating. In the model, proliferating cells are tracked according to position in the cell cycle by assigning to each cell a variable called maturity. Maturity in the control scenario (0 μM lapatinib) corresponds to cell age (i.e. time that has passed since the last mitosis). The maturity values in the control delimiting the phases of the cell cycle are set at $0 - 7\,h$ (G_1), $7 - 11\,h$ (S), and $11 - 30\,h$ (G_2/M) (see Figure 7 **B** and section IV.3 for further explanation). The model takes into account the variability of intermitotic times with mean age of division approximately $19\,h$ in the control (see Figure 7 **A**). The mathematical model was programmed using MATLAB. A standard upwind scheme is used for the numerical solution of the partial differential equations [59].

IV.3 The Mathematical Model

Let $t \geq 0$ denote the time since the beginning of the experiment and $a \in [0, a_1]$ denote the maturity of a cell. This maturity variable can be thought of as the position of a cell in its cell cycle. We wish to emphasize that in the absence of cytostatic effects of drugs, maturity coincides with chronological age, the time since cell division. In experimental terms, maturity is measured by differential DNA–content. See the discussion in [80]

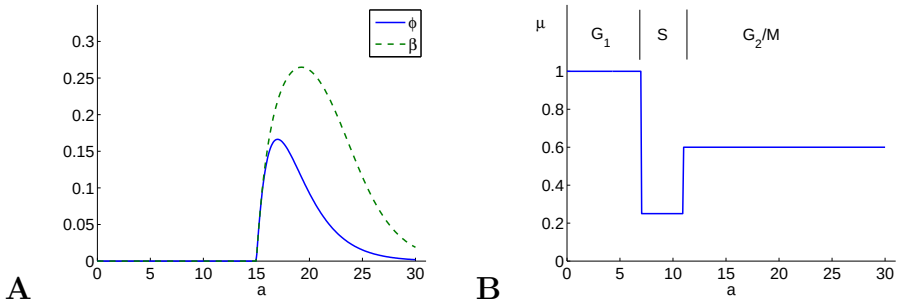

Figure 7: **A** Distribution of intermitotic times φ. **B** The relative tendency to enter the nonproliferating class.

for further information.

Let $p(a,t)$ and $q(a,t)$ denote the densities of proliferating and nonproliferating cells, respectively, of maturity a at time t. The total number of cells at time t is obtained by integrating both densities over the age space

$$N(t) = \int_0^{a_1} (p(a,t) + q(a,t))\,\mathrm{d}a. \tag{35}$$

We state our model equations which balance the biological processes occurring in time

$$\frac{\partial}{\partial t}p(a,t) + \frac{\partial}{\partial a}((1-\delta(a,t))p(a,t)) = -(\beta(a) + \tilde{\mu}(a,N(t)) + \epsilon(t))p(a,t), \tag{36}$$

$$\frac{\partial}{\partial t}q(a,t) = \tilde{\mu}(a,N(t))p(a,t) - \epsilon(t)q(a,t), \tag{37}$$

$$(1-\delta(0,t))p(0,t) = 2\int_0^{a_1} \beta(a)p(a,t)\,\mathrm{d}a, \tag{38}$$

$$p(a,0) = p_0(a),$$

$$q(a,0) = q_0(a).$$

The left hand side of equation (36) describes the aging process for proliferating cells. On the right hand side of the same equation we find that cells of maturity a are lost due to three independent processes. Firstly, cells undergo mitosis, at a rate β

depending on a. Such a cell shows up as two proliferating cells of maturity 0, hence the boundary condition (38). Secondly, proliferating cells are also lost due to a transition into the nonproliferating class. In contrast to proliferating cells, the nonproliferating cells do not mature and do not give rise to new cells. The rate at which the transition between the two classes occurs, $\tilde{\mu}$, depends on the maturity a of the respective cell as well as on the total number of cells N. We set

$$\tilde{\mu}(a, N) = \mu(a) \begin{cases} c(N - N_0) & \text{if } N \geq N_0 \\ 0 & \text{otherwise} \end{cases} . \tag{39}$$

The function $\mu(a)$ is depicted in Figure 7 **B** and its parameters are given in table IV.1. The particular choice of a piecewise constant function is a result of the experimental observations for the control scenario (Figure 8 **B**). Indeed we saw that the percentages of cells in specific phases change after day 4, as more and more cells enter the nonproliferating class. We find it plausible that a cell that has entered S–phase will finish it and therefore be less prone to entering nonproliferation. Thirdly, there is an additional time–dependent cytotoxic effect ϵ for both classes in the presence of drug. We assume the log–kill hypothesis, i.e. the cell kill is proportional to the instantaneous population [67]. Both equations are supplied with initial maturity distributions p_0 and q_0 at time 0.

The cytostatic action of the drug changes the maturation velocity $1 - \delta$ of the proliferating cells. The ordinary differential equation

$$\frac{da}{dt} = 1 - \delta(a, t) \tag{40}$$

describes the characteristic curves of equation (36). Since maturation is irreversible, the function δ must satisfy $0 \leq \delta(a, t) \leq 1$. In the absence of cytostatic effects, we have $\delta = 0$. Then $a - t = const$, that is cells age one–to–one with time, as stated

earlier. On the other hand, if $\delta \approx 1$, cell maturation is (almost) completely blocked. Observe from equation (40) that δ is a dimensionless quantity.

The model predicts the total cell number (35) as well as the percentages of cells in the three stages of the cell cycle. (Cells in G_2– and M–phases are counted together.) These are defined as

$$\begin{aligned} G_1(t) &= \int_0^{a_{G_1}} (p(a,t) + q(a,t))\,\mathrm{d}a \Big/ N(t), \\ S(t) &= \int_{a_{G_1}}^{a_S} (p(a,t) + q(a,t))\,\mathrm{d}a \Big/ N(t), \\ G_2(t) &= \int_{a_S}^{a_1} (p(a,t) + q(a,t))\,\mathrm{d}a \Big/ N(t), \end{aligned} \tag{41}$$

where the boundaries between compartments a_{G_1} and a_S are chosen on the basis of experimental observations and a_1 is the maximum age (see Table IV.1 and Figure 7 **B**). More precisely, the control scenario data were used to fix the parameters a_{G_1} and a_S. We compared the fractions of cells in each phase over time, determined by analysis of DNA content, to the model simulation from equations (41).

Following [17], we have chosen the distribution of intermitotic times φ to be a specific shifted Γ–distribution

$$\varphi(a) = \Phi(a - a_m; \rho, \sigma) = \frac{(a - a_m)e^{-(a-a_m)/\sigma}}{\sigma^2}. \tag{42}$$

Here a_m is the minimal maturity a cell has to reach before it can divide. The parameter σ determines the standard deviation of ϕ (see table IV.1 and Figure 7 **A** for our choice of φ and β). The corresponding age–dependent proliferation rate is given by

$$\beta(a) = \frac{\varphi(a)}{\alpha(a)},$$

where

$$\alpha(a) = \int_a^\infty \varphi(s)\,\mathrm{d}s$$

is the fraction of cells that reach age a without division (see Figure 7 **A**). We allow for a certain percentage to reach maximum age a_1 without division. As argued by Tubiana [79], the mean duration of the cell cycle in solid tumors is relatively constant and therefore not influenced by the total cell number N.

Another source of uncertainty lies in the initial age distributions p_0 and q_0 at time 0. The experimental data indicated that initially proliferating cells in all stages of the cell cycle were present while there were no nonproliferating cells. It should be remarked that in the absence of nonlinear crowding effects one would observe asynchronous exponential growth (see section V.2 for more explanations of this terminology). That is, the total cell number would grow exponentially with a certain well–defined rate λ while the percentage of cells in each age bracket would approach a steady state. This phenomenon has been widely studied in the population dynamics literature; we refer here to [19] and the references therein.

How do we let the drug act on the cells? We want to test the hypothesis that only cells in G_1–phase are blocked while cells in other phases remain unaffected. Hence, we let

$$\delta(a,t) = \delta_{G_1}(d)\frac{t}{T}\begin{cases} 1 \text{ if } 0 \le a \le a_{G_1} \\ 0 \text{ otherwise} \end{cases}, \tag{43}$$

where d is the drug concentration, $\delta_{G_1}(d) \le 1$ is a concentration–dependent rate corresponding to maximum blocking effect and $T = 144\,h$ is the duration of the experiment. We decided to let the action increase linearly with respect to time throughout the entire duration of the experiment. When we tried the simplest way to model time dependence, namely a sudden switch from 0 to a constant $\delta_{G_1} > 0$, the model predicted oscillations in the percentages that were not present in the experimental data. At the higher concentration of $2\,\mu M$ it becomes necessary to introduce an action of the drug on cells in G_2/M–phase, similar to equation (43). In order to explain the decrease of cell counts from day 5 to day 6 we assume that the additional mortality

is of the type

$$\epsilon(t) = \max\{0, \epsilon_0(d) \cdot (t - 120)\}.$$

We list the numerical values of the parameters that are fixed throughout all scenarios in table IV.1. The values of the parameters $\delta_{G_1}(d)$ and $\epsilon_0(d)$ that differ for the specific concentrations are stated in table IV.2.

Table IV.1: Numerical values of the parameters that are fixed throughout all scenarios.

parameter	numerical value	remarks
a_{G_1}	$7\,h$	G_1/S–boundary in absence of drugs
a_S	$11\,h$	S/G_2–boundary in absence of drugs
a_m	$15\,h$	minimal age for division
a_1	$30\,h$	maximal cell age
σ	2	standard deviation of intermitotic times
c	0.22	nonproliferation constant
N_0	$6 \cdot 10^5$ cells	crowding threshold for nonproliferation
$\mu(a)$	{1, 0.25, 0.6}	see Figure 7 **B**

IV.4 Results

In the control scenario (without treatment) the experimental data showed an initial exponential increase of the population and then a leveling off (see Figure 8 **A**). Discrete symbols in Figure 8 mark experimental measurements while continuous curves are the predictions of the model. To explain this leveling off, the nonproliferating cell class was incorporated into the model. Nonlinear models with nonproliferating subpopulations have been used extensively to explain Gompertzian growth kinetics of tumors [24, 25]. Proliferating cells enter the nonproliferating class irreversibly at a rate dependent on their maturity and the total population count of both proliferating and nonproliferating cells. This nonlinearity in the model accounts for the confluence observed in the control study on day 6. Staining of cells with the marker for prolifer-

ation Ki–67 showed a dramatic decrease of the proliferating fraction from 100 % on day 4 to 4% on day 6 (data not shown), well borne out by the numerical simulation (Figure 8 **A**, open circles). In the model, nonproliferating cells arrested their maturity value at the moment of transition from proliferation (see equations (36)–(37)). Notice the observed shift in the cell cycle distribution from day 4 on (Figure 8 **A**). No mortality of cells was assumed in the model for the control, since no decrease in cell numbers was observed. In addition, staining for the marker of apoptosis Caspase–3 was negative for the control (data not shown).

The model for the control case was used as a reference for the treatment cases, with two separate effects of the drug added. The first was the cytostatic effect, which slowed maturation velocity. Our numerical simulations indicate that lapatinib preferentially blocks cells in G_1–phase. At higher concentration ($2\,\mu M$) the model also incorporates blocking effects in G_2/M phase. We find that the strength of the cytostatic effect saturates at higher concentrations (see Table IV.2 and Figure 9 **A**). The second effect of the drug was a cytotoxic action. This was incorporated into the model to explain the decrease in cell counts from day 5 to day 6, which was not present in the control (Figure 10). In the model it was assumed that this cytotoxic action only set in after 5 days. The model simulations agreed substantially with the experimental data, both in the total population counts and the flow cytometric data (Figure 8 **C, D**, where curves for the particular concentration $1\,\mu M$ are shown). Owing to uncertainty in the experimental measurements, there were some discrepancies in the fit, particularly for the flow cytometric data during days $1-3$.

Table IV.2: Cytostatic and cytotoxic effects as functions of drug concentration.

drug concentration (d, μM)	0.1	0.5	1	2
$\delta_{G_1}(d)$	0.3	0.6	0.77	0.92
$\delta_{G_2}(d)$	0	0	0	0.8
$\epsilon_0(d)$	$6 \cdot 10^{-4}$	$1.1 \cdot 10^{-3}$	$1.3 \cdot 10^{-3}$	$1.8 \cdot 10^{-3}$

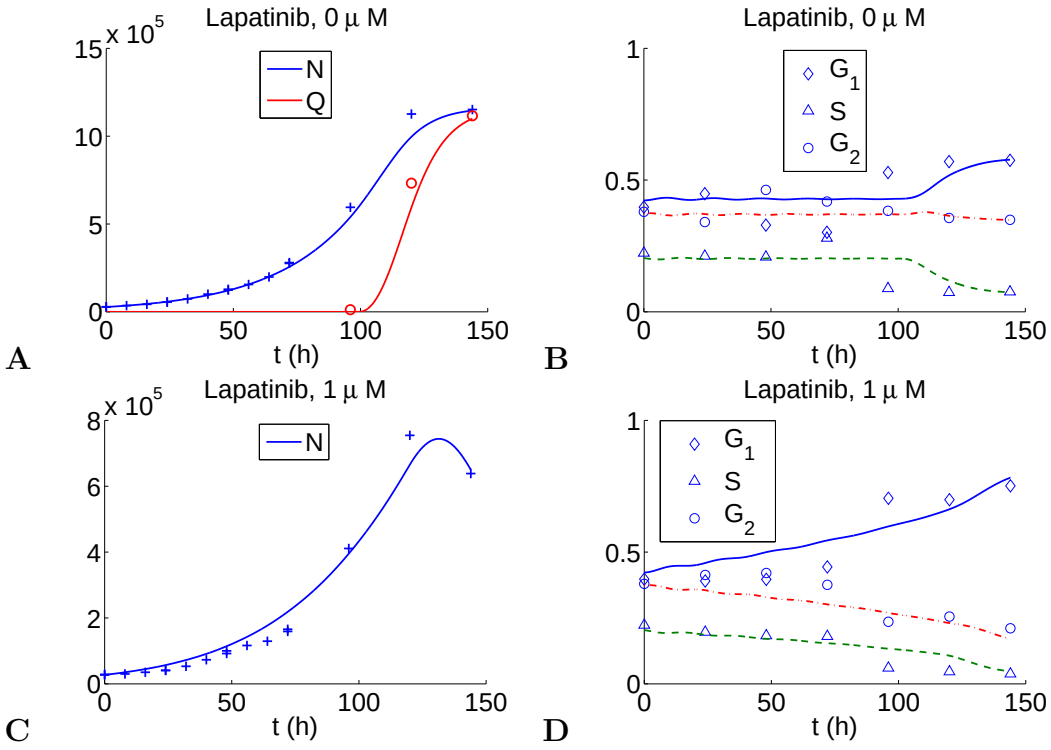

Figure 8: Total cell counts and flow cytometric data for untreated and treated cells.

We find that the dependence of $\delta_{G_1}(d)$ on the drug dosage d is described very well by the equation

$$\delta_{G_1}(d) = \frac{c_1 d}{1 + c_1 d} \tag{44}$$

with $c_1 = 3.5$ (Figure 9 **A**). The effect increases linearly at first and saturates at higher concentrations. A similar behavior can be surmised for the dependence of the cytotoxic effect $\epsilon_0(d)$, which follows

$$\epsilon_0(d) = \frac{c_2 d}{1 + c_3 d} \tag{45}$$

with $c_2 = 4.7 \cdot 10^{-3}$ and $c_3 = 2.1$ (Figure 9 **B**). The functional relationships (44) and (45) are usable for any concentration within a certain range.

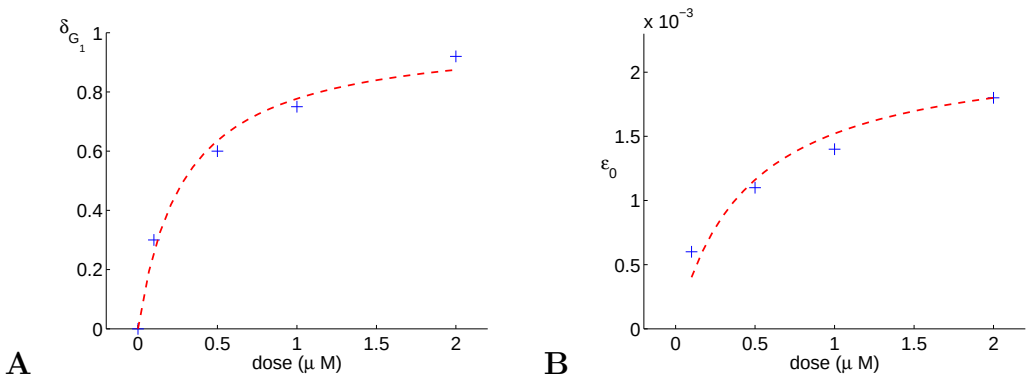

Figure 9: The values $\delta_{G_1}(d)$ **A** and $\epsilon_0(d)$ **B** as functions of concentration.

IV.5 Discussion and Conclusion

The mathematical model provided a means to separate the cytostatic and cytotoxic action of the drug in the experiments. We summarize our findings as follows.

IV.5.1 Cell Cycle Specificity of Cytostatic Effects

The strength of the cytostatic effects depends on the drug dosage; the drug shows saturation kinetics (see the last section and Figure 9 **A** for details). At low concentrations $(0.1 - 1\,\mu M)$ only cells in G_1–phase are delayed. At higher concentrations $(2\,\mu M)$ we hypothesize, on the basis of our model simulations, that cells in G_2–phase are delayed as well and may be prevented from entering mitosis. It was not necessary to introduce a cytostatic effect for cells in S–phase. We therefore suggest that cells in S–phase remain unaffected at all concentrations.

IV.5.2 Dynamic Behavior

Our numerical simulations indicate a buildup phase for the drug action that stretches over several days. Initially we assumed a sudden onset of the cytostatic action after a certain time. The simulations showed pronounced oscillations in the fractions of cells in each phase that were not observed in the data (simulations not shown). We

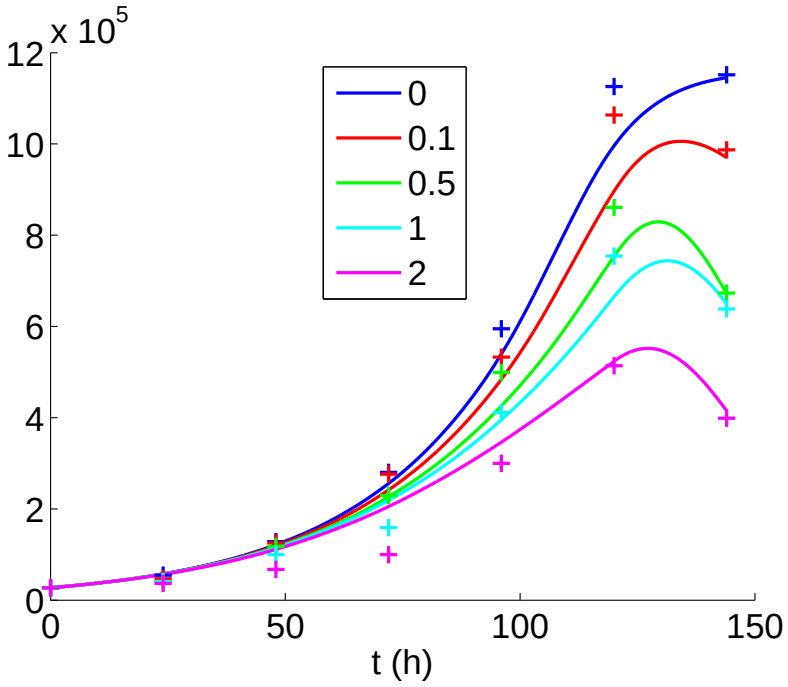

Figure 10: Combined cell counts and simulations for the control and various drug concentrations (in μM).

then assumed a gradual increase (with respect to time) of the cytostatic effects. As the cycle time of an average cell is less than one day, we conjecture that the initial effects of the drugs alters a cell's protein contents but still allows division. Only after several generations is the progression of the cells through the respective cell cycle phases fully retarded. The same holds for the loss of cells. This can be explained by the functional mechanism of the drug and the nature of cell mitosis. Oncogene inhibitors such as lapatinib affect the activities of oncogene downstream effectors, which usually include regulatory proteins crucial for proliferation and survival. As cytoplasmic division occurs during mitosis, the inhibitory effect of lapatinib on these crucial effectors can be "inherited" as protein concentration in the cytosol, where the drug effect can further accumulate. Once the concentrations of these crucial proteins exceed certain thresholds, physiological effects such as growth arrest and apoptosis will be induced in the descendant cells. The conclusions that the length

of lapatinib treatment is crucial for the overall drug effects, and that it takes several cell generations for the drug to show a clear cellular effect, especially at a lower concentration, may have potential clinical implications.

IV.5.3 The Cytotoxic Effect

A model with cytostatic action alone cannot lead to a decrease in total cell number, which made it necessary to introduce a cytotoxic effect. To explain the additional mortality of cells after 120 hours, we propose that cells in which progression through the cell cycle has been retarded for too long become prone to apoptosis in the presence of lapatinib. We conjecture that the strength of the cytotoxic effect also saturates at higher concentrations, as is suggested by Figure 9 **B**.

While it is difficult to extrapolate conclusions from our *in vitro* study to the *in vivo* situation, the following suggestions are plausible. Lapatinib acts chiefly through slowing the progression of proliferating cells in monolayer culture. Furthermore, it is advisable to combine lapatinib with cytotoxic therapeutic agents that kill not only proliferating cells but also quiescent cells, such as some alkylating agents. These drugs may complement the antitumor effect of lapatinib and therefore serve as good candidates to be tested in combined treatment in the future.

We have shown that a mathematical model based on population dynamics can be applied to interpret the cytostatic and cytotoxic effects of lapatinib. Earlier mathematical models [49] used a discrete partition of the cell cycle in age compartments and also a discrete time scale. We find that continuum models are advantageous from the viewpoint of parametrization and computability. In particular, the number of free parameters in our model is significantly smaller than in previously proposed models and each has a straightforward biological interpretation. Our model can certainly be applied to other oncogene inhibitors that have cytostatic effects on cells of a specific phase during the cell cycle.

CHAPTER V

INVESTIGATION OF THE AGE–STRUCTURED MODELS

In this chapter we consider two models for structured populations with proliferating and nonproliferating cells. The first is characterized by the fact that nonproliferating cells do not mature and was used in chapter IV. The second model has aging nonproliferating cells. There the age is the chronological age, the time that has passed since the last mitotic event.

V.1 The Maturity Structured Model

We consider a model for proliferating and nonproliferating cells, structured by a variable that we call *maturity age*. Nonproliferating cells do not mature, they are "stuck" at their last stage in the proliferation cycle. Only a transition from the proliferating to the nonproliferating class is possible and the rate of this transition depends on both age and the total number of cells. The birth process is linear and not affected by the total number of cells.

Our first model consists of the following equations

$$\begin{aligned}
\frac{\partial}{\partial t}p(a,t) + \frac{\partial}{\partial a}p(a,t) &= -(\beta(a) + \sigma(a, N(t)))p(a,t), \\
\frac{\partial}{\partial t}q(a,t) &= \sigma(a, N(t))p(a,t), \\
p(0,t) &= 2\int_0^\infty \beta(a)p(a,t)\,\mathrm{d}a, \\
p(a,0) &= p_0(a), \\
q(a,0) &= q_0(a).
\end{aligned} \tag{46}$$

Here and throughout this chapter

$$N(t) = ||p(t)|| + ||q(t)|| = \int_0^{a_1} (p(a,t) + q(a,t))\,\mathrm{d}a \tag{47}$$

will be the total population[1] with a_1 finite or infinite. The age space will be the half–line $[0,\infty)$ in the first subsection and the bounded interval $[0,a_1]$ in the second. We assume that $\sigma(a,N)$ is nonnegative, not identically zero for every $N > 0$, and increasing with respect to N. We assume throughout this chapter that $\sigma(a,N)$ is Lipschitz continuous with respect to N on bounded subsets, i.e. for $N, \bar{N} \leq M$ there exists a constant $C = C_M$ such that

$$|\sigma(a,N) - \sigma(a,\bar{N}) \leq C|N - \bar{N}|$$

for all $a \in [0,a_1]$. Further, we assume there exists an $\epsilon > 0$ and $N^* > 0$ such that

$$\beta(a) - \sigma(a,N) \leq -\epsilon < 0 \tag{48}$$

for all a and $N \geq N^*$ and an upper bound $\gamma > 0$

$$\sigma(a,N) \leq \gamma \tag{49}$$

for all a and N. These hypotheses will be used to show the global boundedness of p and q later on. We assume that β is measurable, essentially bounded and positive. We assume the compatibility condition for boundary and initial data

$$p_0(0) = 2\int_0^{\infty} \beta(a)p_0(a)\,\mathrm{d}a,$$

for $p_0 \in L^1(0,\infty)$.

[1]Here and in the sequel $||\cdot||$ denotes the L^1–norm, all other norms will be indexed.

There are essentially two ways to show existence of mild solutions to problem (46). One is through Volterra integral equations and is carried out in the book by Iannelli [35]. An alternative way to prove existence of solutions is through semigroups of operators (linear or nonlinear) on a Banach space. The references are the books by Pazy [52] and by Webb [85].

Definition 1. *Let $(Y, ||\cdot||)$ be a Banach space. A family $(U(t))_{t\geq 0}$ of linear, bounded operators is called a strongly continuous semigroup (or a C_0–semigroup) if*

(i) $U(0) = I$,

(ii) $U(t+s) = U(t)U(s)$, *and*

(iii) $\lim_{t\to 0+} ||U(t)y - y|| = 0$ *for all* $y \in Y$.

The influence of the second equation of (46) on the first is very weak in the sense that

$$\sigma(a, ||p|| + ||q||) \geq \sigma(a, ||p||),$$

thus a presence of nonproliferating cells only increases the loss rate for proliferating cells. Let $Y = L^1(0,\infty)$ with positive cone

$$Y_+ = \{p \in Y \ : \ p \geq 0 \text{ a. e. } \}$$

and define

$$D(A) = \left\{ p \in W^{1,1}(0,\infty) \ : \ p(0) = 2\int_0^\infty \beta(a)p_0(a)\,\mathrm{d}a \right\},$$
$$Ap = -(p' + \beta p).$$

The domain $D(A)$ is dense in Y [85, Proposition 3.8], and A is a closed operator [57]. Furthermore, A is the infinitesimal generator of a positive C_0–semigroup $(U(t))_{t\geq 0}$ on the Banach space Y, i.e. Y_+ is invariant under U [57]. The semigroup U has the

growth bound

$$||U(t)|| \leq e^{||\beta||_\infty t}.$$

Now we consider the abstract nonlinear equation

$$\begin{aligned} \frac{d}{dt}p &= Ap + F(p), \\ p(0) &= p_0, \end{aligned} \tag{50}$$

with $p_0 \in Y_+$. The nonlinearity has the form $F : Y \to Y$,

$$F(p) = -\sigma(\,\cdot\,, ||p||)p, \quad p \in Y. \tag{51}$$

The nonlinearity F satisfies a Lipschitz condition with respect to p on bounded sets, by the assumptions on σ. The unique mild solution $p(t) \in Y_+$ of (50) is given by

$$p(t) = U(t)p_0 + \int_0^t U(t-s)F(p(s))\,\mathrm{d}s.$$

F is bounded ($F(B)$ is bounded for all bounded sets $B \subset Y$) and satisfies

$$(F(p), p)_- \leq 0,$$

where the semi–inner product is defined by

$$(u, v)_- = \min\{(u, v^*) \,:\, v^* \in Y^*, ||v^*|| = ||v||, (v, v^*) = ||v||^2\}.$$

Therefore, [57, Theorem B (iii)] guarantees that mild solutions exist for all t, they remain positive for positive initial valueas, depend continuously of the initial value p_0 and satisfy a growth estimate

$$||p(t)|| \leq ||p_0||e^{||\beta||_\infty t}.$$

Moreover, if σ is differentiable with respect to N and $p_0 \in D(A) \cap Y_+$ then the mild solution is also a strong solution, i.e. $p(t) \in C^1([0,\infty); D(A) \cap Y_+)$ and the differential equation (46) is satisfied.

We will now show that solutions to model (46) remain bounded. As abbreviations we set $P(t) = ||p(\cdot\,, t)||$ and $Q(t) = ||q(\cdot\,, t)||$.

Theorem V.1.1. *Let the conditions* (48) *and* (49) *hold and let* (p, q) *be a strong solution of* (46)*. Then*

$$\bar{P} = \lim_{t\to\infty} P(t) \tag{52}$$

and

$$\bar{Q} = \lim_{t\to\infty} Q(t) \tag{53}$$

exist and are finite.

Proof. Assume that $N(t) \to \infty$ as $t \to \infty$. Since

$$N'(t) = \int_0^\infty \beta(a)p(a,t)\,\mathrm{d}a \geq 0$$

(for a strong solution $N'(t)$ exists), N is nondecreasing. Thus there exists a time t_1 such that $N(t) \geq N^*$ for all $t \geq t_1$. Using condition (48) we find the estimate

$$P'(t) = \int_0^\infty (\beta(a) - \sigma(a, N(t)))p(a,t)\,\mathrm{d}a \leq -\epsilon P(t)$$

for $t \geq t_1$ and therefore

$$P(t) \leq e^{-\epsilon(t-t_1)}P(t_1)$$

for $t \geq t_1$. Hence P remains bounded. For the rate of change of Q we have the estimate

$$Q'(t) = \int_0^\infty \sigma(a, N(t))p(a,t)\,\mathrm{d}a \leq \gamma P(t) \leq e^{-\epsilon(t-t_1)}P(t_1)$$

for $t \geq t_1$, where we have used condition (49). Thus

$$Q(t) \leq Q(t_1) + \frac{\gamma P(t_1)}{\epsilon}\left(1 - e^{-\epsilon(t-t_1)}\right)$$

for $t \geq t_1$. In summary, $N(t) = P(t) + Q(t)$ is bounded and increasing, let

$$\bar{N} = \lim_{t\to\infty} N(t).$$

Since $Q'(t) \geq 0$ and $Q(t) \leq \bar{N}$, the limit of $Q(t)$ as $t \to \infty$ exists and the claim (53) is shown. Finally

$$\lim_{t\to\infty} P(t) = \lim_{t\to\infty} N(t) - \lim_{t\to\infty} Q(t) = \bar{N} - \bar{Q},$$

the claim (52) holds. □

V.2 The Model with Aging Nonproliferating Cells

In the model (46) the nonproliferating cells do not mature. An alternative model was proposed by Arino et al. [4, 19]. In that model, the age variable has the interpretation of *chronological age*, that is the time since the last mitotic event.

The equations for proliferating and nonproliferating cells are

$$\begin{aligned}
\frac{\partial}{\partial t}p(a,t) + \frac{\partial}{\partial a}p(a,t) &= -(\beta(a) + \sigma(a,N(t)))p(a,t) + \tau(a,N(t))q(a,t),\\
\frac{\partial}{\partial t}q(a,t) + \frac{\partial}{\partial a}q(a,t) &= \sigma(a,N(t))p(a,t) - \tau(a,N(t))q(a,t),\\
p(0,t) &= 2f\int_0^{a_1} \beta(a)p(a,t)\,\mathrm{d}a,\\
q(0,t) &= 2(1-f)\int_0^{a_1} \beta(a)p(a,t)\,\mathrm{d}a,\\
p(a,0) &= p_0(a),\\
q(a,0) &= q_0(a).
\end{aligned} \tag{54}$$

The age space is now the finite interval $[0, a_1]$. Individuals can move back and forth between the proliferating and nonproliferating classes, at rates that depend on the total population defined as in equation (47). For fixed N we assume that the functions $\sigma(\,\cdot\,, N)$ and $\tau(\,\cdot\,, N)$ are bounded and measurable. The constant $0 < f \leq 1$ determines the probability of entering the proliferating class upon birth. The birth rate satisfies $\beta \in L^\infty(0, a_1)$. Loss of cells occurs through proliferating and nonproliferating cells that reach the maximum age a_1. For fixed a we assume that $\sigma(a, \,\cdot\,)$ is increasing, $\tau(a, \,\cdot\,)$ is decreasing and that both functions are Lipschitz continuous (with respect to N) on bounded sets. We define

$$D(\mathcal{A}) = \Big\{(p,q) \in W^{1,1}(0,a_1) \times W^{1,1}(0,a_1) \,:\, p(0) = 2f \int_0^{a_1} \beta(a)p(a)\,\mathrm{d}a,$$
$$q(0) = 2(1-f)\int_0^{a_1} \beta(a)p(a)\,\mathrm{d}a\Big\},$$
$$\mathcal{A} = \begin{pmatrix} -\left(\frac{\partial}{\partial a} + \beta\right) & 0 \\ 0 & -\frac{\partial}{\partial a} \end{pmatrix}$$

and

$$F\begin{pmatrix} p \\ q \end{pmatrix} = \begin{pmatrix} -\sigma(a, N(t)) & \tau(a, N(t)) \\ \sigma(a, N(t)) & -\tau(a, N(t)) \end{pmatrix}\begin{pmatrix} p \\ q \end{pmatrix}.$$

Let U be the positive C_0–semigroup generated by the operator $\mathcal{A}$. We consider the nonlinear problem (51) with the new choices for $\mathcal{A}$ and F. It was shown in [19] that the C_0–semigroup corresponding to the linear problem (i.e. where σ and τ are independent of N) possesses the property of asynchronous exponential growth, which we are going to define now. The following assumptions are made in [19], that we adopt as well for the remainder of this section. There exists $\epsilon_0 > 0$ such that

$$\int_{a_1-\epsilon}^{a_1} \beta(a)\,\mathrm{d}a > 0, \tag{55}$$

for all $0 < \epsilon < \epsilon_0$. That is, the oldest cells in the proliferating class are still able to

proliferate. This avoids trivial cases where the support of the initial datum p_0 lies beyond the support of β (this would result in a complete loss of proliferating cells). In addition

$$\int_{a_1-\epsilon}^{a_1} \tau(a)\,\mathrm{d}a > 0 \tag{56}$$

for all $0 < \epsilon < \epsilon_0$. That is, the oldest cells in the proliferating class still proliferate and the oldest nonproliferating cells can still return to the proliferating class. If $f = 1$ then the additional assumption

$$\int_0^{\epsilon} \sigma(a)\,\mathrm{d}a > 0 \tag{57}$$

for all $0 < \epsilon < \epsilon_0$ is made. That means, some of the youngest proliferating cells can exit their class. Roughly speaking, conditions (55) and (56) guarantee the "spreading" over the entire age space of a population that initially consists only of old proliferating or only of nonproliferating cells. Condition (57) guarantees that nonproliferating cells of all ages will occur, in case all cells are born proliferating.

Definition 2. *A semigroup $U(t)$ on the Banach space X has asynchronous exponential growth if there exists $\lambda \in \mathbb{R}$ and a rank one projection P_0 on X such that*

$$\lim_{t\to\infty} e^{-\lambda t} U(t)x = P_0 x$$

for all $x \in X$.

In the context of population dynamics the parameter λ is commonly known as the *Malthusian* or *intrinsic* growth parameter. It was shown in [19, Theorem 2] that the linear semigroup $V(t)$ associated with the problem (54), but with σ and τ independent of N has asynchronous exponential growth. Moreover, the parameter λ is determined

as follows. Let $W : [0, a_1] \to M_2$, the set of positive real 2×2 matrices

$$W(a) = \begin{pmatrix} w_{11}(a) & w_{12}(a) \\ w_{21}(a) & w_{22}(a) \end{pmatrix}$$

be the solution of the matrix ordinary differential equation

$$W'(a) = \begin{pmatrix} -(\beta(a) + \sigma(a)) & \tau(a) \\ \sigma(a) & -\tau(a) \end{pmatrix} W(a), \quad W(0) = I.$$

Then λ is the unique solution of the characteristic equation

$$\int_0^{a_1} 2\beta(a) e^{-\lambda a} (f w_{11}(a) + (1 - f) w_{12}(a)) \, \mathrm{d}a = 1. \tag{58}$$

Notice that the parameter λ is completely determined by the parameters of the problem σ, τ and β and it may be either positive or negative.

In [19] the authors raised the question how the growth behavior would change for transition functions σ and τ that are nonlinearly dependent on the total population. We want to show in the remainder of this section that nontrivial equilibrium solutions exist.

To find an equilibrium solution of (54) we set the time derivative in the first two equations of (54) to zero. Let

$$B(a, N) = \begin{pmatrix} -(\beta(a) + \sigma(a, N)) & \tau(a, N) \\ \sigma(a, N) & -\tau(a, N) \end{pmatrix}.$$

By our assumptions on the Lipschitz continuity of σ and τ and the boundedness of β, $B(a, N)$ is clearly a continuous and bounded matrix function with respect to N.

We obtain the ordinary differential equation

$$\begin{pmatrix} p \\ q \end{pmatrix}' = B(a,N) \begin{pmatrix} p \\ q \end{pmatrix}(a),$$

where

$$N = \int_0^{a_1} (p(a) + q(a))\,\mathrm{d}a = ||p|| + ||q||.$$

Let

$$W(a,N) = \begin{pmatrix} w_{11}(a,N) & w_{12}(a,N) \\ w_{21}(a,N) & w_{22}(a,N) \end{pmatrix} \in M_2$$

be the fundamental solution of the matrix ordinary differential equation [16, chapter 3, section 2]

$$W'(a,N) = B(a,N)W(a,N), \quad W(0,N) = I.$$

Closely related to the Malthusian growth parameter from equation (58) is the net reproductive rate at constant population N which is given by

$$R(N) = 2\int_0^{a_1} \beta(a)(f w_{11}(a,N) + (1-f)w_{12}(a,N))\,\mathrm{d}a,$$

compare this to [19, Theorem 2]. Notice that $R(N)$ is completely determined by the parameters of the problem σ, τ and β and may be greater or less than 1. For given (p^0, q^0) and N set

$$\begin{pmatrix} P \\ Q \end{pmatrix}(a) = W(a,N) \begin{pmatrix} p^0 \\ q^0 \end{pmatrix}. \tag{59}$$

Note that $\begin{pmatrix} P \\ Q \end{pmatrix}(a) \in \mathbb{R}^2_+$. Clearly

$$\begin{pmatrix} P \\ Q \end{pmatrix}'(a) = B(a,N)\begin{pmatrix} P \\ Q \end{pmatrix}(a), \quad \begin{pmatrix} P \\ Q \end{pmatrix}(0) = \begin{pmatrix} p^0 \\ q^0 \end{pmatrix}.$$

We notice for further use that P and P' are bounded on bounded sets of arguments p^0, q^0, N and $0 \le a \le a_1$

$$|P(a)| \le C_1, \quad |P'(a)| \le C_2, \tag{60}$$

the same holds for Q and Q'.

We can now reformulate the problem of finding an equilibrium solution to problem (54) as a fixed point problem. Let X be the Banach space $X = L^1(0,a_1)^2 \times \mathbb{R}^2$ with norm

$$||(p,q,p^0,q^0)||_X = ||p|| + ||q|| + |p^0| + |q^0|$$

and let C be the standard positive cone in X. For a 4–tuple $(p,q,p^0,q^0) \in C$ define

$$\mathcal{T}(p,q,p^0,q^0) = \begin{pmatrix} P(\,\cdot\,;p,q,p^0,q^0) \\ Q(\,\cdot\,;p,q,p^0,q^0) \\ 2f\int_0^{a_1}\beta(a)P(a;p,q,p^0,q^0)\,\mathrm{d}a \\ 2(1-f)\int_0^{a_1}\beta(a)P(a;p,q,p^0,q^0)\,\mathrm{d}a \end{pmatrix},$$

where P and Q are defined as in equation (59) with $N = ||p|| + ||q||$. Since $\mathcal{T}$ is a composition of bounded and continuous maps it is itself bounded and continuous with respect to all its arguments. We look for a fixed point in C,

$$\mathcal{T}(p,q,p^0,q^0) = (p,q,p^0,q^0).$$

We proceed as in the proof of and [58, Theorem 1] and [85, Theorem 4.1]. There, the following theorem due to H. Amann [3, Theorem 12.3] is used.

Theorem V.2.1. *Let X be a Banach space, let C be a closed convex cone in X, let $\gamma > 0$ and set $C_\gamma = C \cap B_X(0, \gamma)$. Suppose $f : C_\gamma \to C$ is a continuous map and $f(C_\gamma)$ is relatively compact. Assume further that*

(i) $f(x) \neq \lambda x$ for all $x \in C_\gamma$ with $||x|| = \gamma$ and all $\lambda > 1$, and

(ii) there exists $\delta \in (0, \gamma)$ and $x_1 \in C, x_1 \neq 0$, such that

$$x - f(x) \neq \lambda x_1$$

for all $x \in C$ with $||x|| = \delta$ and all $\lambda > 0$.

Then f has a fixed point $x_0 \in C$ with $\delta \leq ||x_0|| \leq \gamma$.

We need conditions to guarantee that both 0 and ∞ are repelling, i.e. that the total population does not die out or grows beyond every bound. These conditions are

(a) There exists $N_* > 0$ such that the triple $(\sigma(\,\cdot\,, N), \tau(\,\cdot\,, N), \beta)$ has the property that $R(N) > 1$ for all $N \leq N_*$.

(b) There exists $N^* > N_*$ such that the triple $(\sigma(\,\cdot\,, N), \tau(\,\cdot\,, N), \beta)$ has the property that $R(N) < 1$ for all $N \geq N^*$.

These conditions are quite natural, as a small population is expected to grow while a large population is expected to shrink. We state the theorem.

Theorem V.2.2. *Let conditions (a) and (b) be satisfied. Then there exists at least one nontrivial equilibrium solution of* (54).

Proof. We fix $\gamma = N^*(1 + 2||\beta||_\infty)$. The map $\mathcal{T}$ was shown to be continuous and bounded earlier. The image $\mathcal{T}(C_\gamma)$ has compact closure as will be shown now. We

use Kolmogorov's criterion for compactness in L^1, [18, Theorem 20.3]. It says that a closed and bounded set $M \subset L^1(0, a_1)$ is compact if and only if

$$\lim_{h \to 0} \int_0^{a_1} |\phi(a+h) - \phi(a)| \, \mathrm{d}a = 0, \tag{61}$$

uniformly in h, for all $\phi \in M$. Here we define $\phi(a+h) = 0$ if $a + h \notin [0, a_1]$. To show (61) for $P(\,\cdot\,; p, q, p^0, q^0) \in M =: \mathcal{T}(C_\gamma))$, let $h > 0$ and compute

$$\begin{aligned}
\int_0^{a_1} |P(a+h) - P(a)| \, \mathrm{d}a &= \int_0^{a_1 - h} |P(a+h) - P(a)| \, \mathrm{d}a + \int_{a_1 - h}^{a_1} |P(a)| \, \mathrm{d}a \\
&\leq \int_0^{a_1 - h} \int_a^{a+h} |P'(b)| \, \mathrm{d}b \, \mathrm{d}a + \int_{a_1 - h}^{a_1} |P(a)| \, \mathrm{d}a \\
&\leq h(C_2 a_1 + C_1),
\end{aligned}$$

where we use the bounds provided by (60) and (61) follows. (The bounds from (60) continue to hold for the closure of $\mathcal{T}(C_\gamma)$.) The case $h < 0$ is treated analogously and (61) holds for the function Q as well.

We show condition (i) of Theorem 2. Suppose there exists $\lambda > 1$ such that

$$\lambda(p, q, p^0, q^0) = \mathcal{T}(p, q, p^0, q^0)$$

with $||(p, q, p^0, q^0)||_X = \gamma$. Observe that in this case

$$q^0 = p^0 \frac{1 - f}{f}.$$

If $p^0 = 0$ then it would follow $q^0 = 0$ and hence $p \equiv q \equiv 0$ by equation (59). Thus $p^0 \neq 0$ and

$$\begin{aligned}\lambda p^0 &= 2f \int_0^{a_1} \beta(a) P(a; p, q, p^0, q^0)\, \mathrm{d}a \\ &= 2f \int_0^{a_1} \beta(a)(p^0 w_{11}(a, N) + q^0 w_{12}(a, N))\, \mathrm{d}a \\ &= 2p^0 \int_0^{a_1} \beta(a)(f w_{11}(a, N) + (1 - f) w_{12}(a, N))\, \mathrm{d}a = p^0 R(N)\end{aligned} \tag{62}$$

implies that $\lambda = R(N) > 1$. By assumption (b), $||p|| + ||q|| < N^*$. It follows

$$\begin{aligned}\gamma &= ||p|| + ||q|| + p^0 + q^0 < N^* + 2\lambda^{-1} \int_0^{a_1} \beta(a) P(a; p, q, p^0, q^0)\, \mathrm{d}a \\ &= N^* + 2 \int_0^{a_1} \beta(a) p(a)\, \mathrm{d}a \leq N^*(1 + 2||\beta||_\infty) \stackrel{!}{=} \gamma.\end{aligned}$$

This is a contradiction, by the choice of γ.

Finally, to show condition (ii) of Theorem 2, choose $\delta = N_*$ and $x_1 = (0, 0, 1, 0)$. Assume there exists $\lambda > 0$ such that

$$(p, q, p^0, q^0) - \mathcal{T}(p, q, p^0, q^0) = \lambda x_1$$

with $||(p, q, p^0, q^0)||_X = \delta$. Then, as in equation (62)

$$p^0 - 2f \int_0^{a_1} \beta(a) P(a; p, q, p^0, q^0)\, \mathrm{d}a = \lambda.$$

This implies $p^0(1 - R(||p|| + ||q||)) = \lambda > 0$. By assumption (a), $R(||p|| + ||q||) > 1$ and thus $p^0 < 0$. This is a contradiction to the assumed positivity. The conditions of Theorem 2 are satisfied and a nontrivial equilibrium solution of problem (54) exists. □

CHAPTER VI

CONCLUSION AND OUTLOOK

In summary, we have used successfully partial differential equation models to study a range of diverse phenomena. While age–structured population models been used for more than 80 years [47, 66], their application to growing of cell populations – to the best of our knowledge – new.

As this thesis is being prepared and submitted we have just started a new collaboration with Emily Wang and Glenn Webb. The goal is to investigate the pro– and antitumor effects of the transformed growth factor TGF–β. It is known from biological experiments that TGF–β on the one hand increases the motility of cells (thereby potentially promoting invasion and metastasis) and on the other hand slows down the growth of cells. We have developed a mathematical model based on the Kolmogorov–Fisher equation

$$\frac{\partial}{\partial t}u(x,t) = D\Delta u(x,t) + \alpha u(1-\beta u). \tag{63}$$

Here D denotes the diffusion constant and α the growth rate. It is well known that equation (63) exhibits traveling wave solutions [41]. What makes this model interesting and challenging is the fact that both proliferation and random motility contribute to the spatial spread of the cell population. Thus both effects must be incorporated into the diffusion constant D in equation (63). Experiments are currently underway to determine the influence of TGF–β on the random motility of MCF10A cells and also its effects on cell–cell adhesion. At later stages we plan to include further variables such as extracellular matrix and matrix–degrading enzymes.

BIBLIOGRAPHY

[1] Alekseev, A. S. and V. S. Belonosov. Direct and inverse problems of wave propogation through a one dimensional inhomogeneous medium. *European J. Appl. Math.*, **10**:79–96, 1999.

[2] Alimandi, M., A. Romano, M. C. Curia, R. Muraro, P. Fedi, S. A. Aaronson, P. P. Di Fiore, and M. H. Kraus. Cooperative signaling of ErbB3 and ErbB2 in neoplastic transformation and human mammary carcinomas. *Oncogene*, **10**:1813–1821, 1995.

[3] Amann, H. Fixed point equations and nonlinear eigenvalue problems in ordered Banach spaces. *SIAM Rev.*, **18**:620–709, 1976.

[4] Arino, O., E. Sánchez, and G. F. Webb. Necessary and sufficient conditions for asynchronous exponential growth in age structured cell populations with quiescence. *J. Math. Anal. Appl.*, **215**:499–513, 1997.

[5] Banks, H. T. and B. G. Fitzpatrick. Statistical methods for model comparison in parameter estimation problems for distributed systems. *J. Math. Biol.*, **28**:501–527, 1990.

[6] Belinskiy, B. P. and P. Caithamer. Energy of a string driven by a two–parameter gaussian noise white in time. *J. Appl. Probab.*, **38**:960–974, 2001.

[7] Belinskiy, B. P. and P. Caithamer. Energy of an elastic mechanical system driven by Gaussian noise white in time. *Discrete Contin. Dynam. Systems*, **Added Volume**:39–49, 2001.

[8] Bertuzzi, A., A. D'Onofrio, A. Fasano, and A. Gandolfi. Regression and regrowth of tumour cords following single–dose anticancer treatment. *Bull. Math. Biol.*, **65**:903–931, 2003.

[9] Bishop, T. C., R. Cortez, and O. O. Zhmudsky. Investigation of bend and shear waves in a geometrically exact elastic rod model. *J. Comput. Phys.*, **193**:642–665, 2004.

[10] Braga, J., J. M. P. Desterro, and M. Carmo–Fonseca. Intracellular macromolecular mobility measured by fluorescence recovery after photobleaching with confocal laser scanning microscopes. *Mol. Biol. Cell*, **15**:4749–4760, 2004.

[11] Burridge, R. The Gelfand–Levitan, the Marchenko, and the Gopinath–Sondhi integral equations of inverse scattering theory, regarded in the context of inverse impulse problems. *Wave Motion*, **2**:305–323, 1980.

[12] Carrero, G., E. Crawford, M. J. Hendzel, and G. de Vries. Characterizing fluorescence recovery curves for nuclear proteins undergoing binding events. *Bull.*

Math. Biol., **66**:1515–1545, 2004.

[13] Carrero, G., E. Crawford, J. Th'ng, G. de Vries, and M. J. Hendzel. Quantification of protein–protein and protein–DNA interactions in vivo, using fluorescence recovery after photobleaching. *Methods in Enzymology*, **375**:415–442, 2003.

[14] Carrero, G., D. McDonald, E. Crawford, G. de Vries, and M. J. Hendzel. Using FRAP and mathematical modeling to determine the in vivo kinetics of nuclear proteins. *Methods*, **29**:14–28, 2003.

[15] Chène, P. The role of tetramerization in p53 function. *Oncogene*, **20**:2611–2617, 2001.

[16] Coddington, E. A. and N. Levinson. *Theory of Ordinary Differential Equations*. McGraw–Hill, New York, 1955.

[17] Dibrov, B. F., A. M. Zhabotinsky, Yu. A. Neyfakh, M. P. Orlova, and L. I. Churikova. Optimal scheduling for cell synchronization by cycle–phase–specific blockers. *Math. Biosci.*, **66**:167–185, 1983.

[18] Dunford, N. and J. T. Schwartz. *Linear operators, Part I.* John Wiley & Sons, New York, 1958.

[19] Dyson, J., R. Villella–Bressan, and G. F. Webb. Asynchronous exponential growth in an age structured population of proliferating and quiescent cells. *Math. Biosci.*, **177/178**:73–83, 2002.

[20] Einstein, A. Über die von der molekularkinetischen Theorie der Wärme geforderte Bewegung von in ruhenden Flüssigkeiten suspendierten Teilchen. *Ann. Phys.*, **17**:549–560, 1905.

[21] Engl, H. W., M. Hanke, and A. Neubauer. *Regularization of Inverse Problems*. Kluwer Academic Publishers, Dordrecht, Boston, 1996.

[22] Friedman, P. N., X. B. Chen, J. Bargonetti, and C. Prives. The p53 protein is an unusually shaped tetramer that binds directly to DNA. *Proc. Natl. Acad. Sci. U.S.A.*, **90**:3319–3323, 1993.

[23] Gowers, D. M., G. G. Wilson, and S. E. Halford. Measurement of the contributions of 1D and 3D pathways to the translocation of a protein along DNA. *Proc. Natl. Acad. Sci. USA*, **102**:15883–15888, 2005.

[24] Gyllenberg, M. and G. F. Webb. Quiescence as an explanation of gompertzian tumor growth. *Growth Develop. Aging*, **53**:25–33, 1989.

[25] Gyllenberg, M. and G. F. Webb. A nonlinear structured population model of tumor growth with quiescence. *J. Math. Biol.*, **28**:671–694, 1990.

[26] Halford, S. E. and J. F. Marko. How do site-specific DNA–binding proteins find

their targets. *Nucleic Acids Research*, **32**:3040–3052, 2004.

[27] Harari, D. and Y. Yarden. Molecular mechanisms underlying ErbB2/HER2 action in breast cancer. *Oncogene*, **19**:6102–6114, 2000.

[28] Hinow, P. Some remarks about Brownian motion, diffusion, and anomalous diffusion. Qualifying paper, Vanderbilt University, 2004.

[29] Hinow, P. and E. M. Boczko. Molecular seismology: An inverse problem in nanobiology. *J. Theor. Biol.*, **246**:145–158, 2006.

[30] Hinow, P., C. E. Rogers, C. E. Barbieri, J. A. Pietenpol, A. K. Kenworthy, and E. DiBenedetto. The DNA binding activity of p53 displays reaction–diffusion kinetics. *Biophys. J.*, **91**:330–342, 2006.

[31] Hinow, P., S. Wang, C. L. Arteaga, and G. F. Webb. A mathematical model separates quantitatively the cytostatic and cytotoxic effects of a HER2 tyrosine kinase inhibitor. *Theor. Biol. Med. Model.*, **4**:14, 2007.

[32] Houtsmuller, A. B., S. Rademakers, A. L. Nigg, D. Hoogstraten, J. H. J. Hoeijmakers, and W. Vermeulen. Action of DNA repair endonuclease ERCC1/XPF in living cells. *Science*, **284**:958–961, 1999.

[33] Houtsmuller, A. B. and W. Vermeulen. Macromolecular dynamics in living cell nuclei revealed by fluorescence redistribution after photobleaching. *Histochem. Cell Biol.*, **115**:13–21, 2001.

[34] Hynes, N. E. and D. F. Stern. The biology of erbB–2/neu/HER–2 and its role in cancer. *Biochim. Biophys. Acta*, **1198**:165–184, 1994.

[35] Iannelli, M. *Mathematical Theory of Age–structured Population Dynamics*. Giardini, Pisa, 1995.

[36] Isakov, V. *Inverse Problems for Partial Differential Equations*. Springer Verlag, New York, 1998.

[37] Johnston, S. R. and A. Leary. Lapatinib: a novel EGFR/HER2 tyrosine kinase inhibitor for cancer. *Drugs Today (Barc)*, **42**:441–453, 2006.

[38] Kheifetz, Y., Y. Kogan, and Z. Agur. Long–range predictability in models of cell populations subjected to phase–specific drugs: growth–rate approximation using properties of positive compact operators. *preprint*, 2006.

[39] Kimmel, M. and A. Świerniak. Using control theory to make cancer chemotherapy beneficial from phase dependence and resistant to drug resistance. *Arch. Control. Sci.*, **14**:105–145, 2004.

[40] A. Kirsch. *An introduction to the mathematical theory of inverse problems*. Springer Verlag, New York, 1996.

[41] Kolmogorov, A. N., I. G. Petrovskii, and N. S. Piskunov. A study of the equation of diffusion with increase in the quantity of matter, and its application to a biological problem. *Bull. Moscow Univ.*, **1**:1–25, 1937. English translation in P. Pelcé, editor, *Dynamics of Curved Fronts.* Academic Press, San Diego, 1988.

[42] Konecny, G. E., M. D. Pegram, N. Venkatesan, R. Finn, G. Yang, M. Rahmeh, M. Untch, D. W. Rusnak, G. Spehar, R. J. Mullin, B. R. Keith, T. M. Gilmer, M. Berger, K. C. Podratz, and D. J. Slamon. Activity of the dual kinase inhibitor lapatinib (GW572016) against HER–2–overexpressing and trastuzumab–treated breast cancer cells. *Cancer Res.*, **66**:1630–1639, 2006.

[43] Le, X. F., I. Betrosian, W. Mao, M. Murray, Z. Lu, K. Keyomarsi, M. H. Lee, J. Zhao, and R. C. Bast. Anti–HER2 antibody trastuzumab inhibits CDK2–mediated NPAT and histone H4 expression via the PI3K pathway. *Cell Cycle*, **5**:1654–1661, 2006.

[44] Lupi, M., P. Cappella, G. Matera, C. Natoli, and P. Ubezio. Interpreting cell cycle effects of drugs: the case of melphalan. *Cancer Chemother. Pharmacol.*, **57**:443–457, 2006.

[45] Lupi, M., G. Matera, D. Branduardi, M. D'Incalci, and P. Ubezio. Cytostatic and cytotoxic effects of topotecan decoded by a novel mathematical simulation approach. *Cancer Res.*, **64**:2825–2832, 2004.

[46] Magni, P., M. Simeoni, I. Poggesi, M. Rocchetti, and G. De Nicolao. A mathematical model to study the effects of drugs administration on tumor growth dynamics. *Math. Biosci.*, **200**:127–151, 2006.

[47] McKendrick, A. G. Applications of mathematics to medical problems. *Proc. Edin. Math. Soc.*, **44**:98–130, 1926.

[48] Misteli, T. Protein dynamics: implications for nuclear architecture and gene expression. *Science*, **291**:843–847, 2001.

[49] Montalenti, F., G. Sena, P. Cappella, and P. Ubezio. Simulating cancer–cell kinetics after drug treatment: application to cisplatin on ovarian carcinoma. *Phys. Rev. E*, **57**:5877–5887, 1998.

[50] Muthuswamy, S. K., D. Li, S. Lelievre, M. J. Bissell, and J. S. Brugge. ErbB2, but not ErbB1, reinitiates proliferation and induces luminal repopulation in epithelial acini. *Nat. Cell Biol.*, **3**:785–792, 2001.

[51] Nelson, M. H. and C. R. Dolder. Lapatinib: a novel dual tyrosine kinase inhibitor with activity in solid tumors. *Ann. Pharmacother.*, **40**:261–269, 2006.

[52] Pazy, A. *Semigroups of Linear Operators and Applications to Partial Differential Equations.* Springer–Verlag, New York, 1983.

[53] Phair, R. D., S. A. Gorski, and T. Misteli. Measurement of dynamic protein

binding to chromatin in vivo, using photobleaching microscopy. *Methods in Enzymology*, **375**:393–414, 2003.

[54] Phair, R. D. and T. Misteli. High mobility of proteins in the mammalian cell nucleus. *Nature*, **404**:604–609, 2000.

[55] Phair, R. D., P. Scaffidi, C. Elbi, J. Vecerová, A. Dey, K. Ozato, D. T. Brown, G. Hager, M. Bustin, and T. Misteli. Global nature of dynamic protein–chromatin interactions in vivo: three–dimensional genome scanning and dynamic interaction networks of chromatin proteins. *Mol. Cell. Biol.*, **24**:6393–6402, 2004.

[56] Pierce, J. H., P. Arnstein, E. DiMarco, J. Artrip, M. H. Kraus, F. Lonardo, P. P. Di Fiore, and S. A. Aaronson. Oncogenic potential of erbB–2 in human mammary epithelial cells. *Oncogene*, **6**:1189–1194, 1991.

[57] Prüss, J. Equilibrium solutions of age–specific population dynamics of several species. *J. Math. Biol.*, **11**:65–84, 1981.

[58] Prüss, J. On the qualitative behaviour of populations with age–specific interactions. *Comput. Math. Appl.*, **9**:327–339, 1983.

[59] Quarteroni, A., R. Sacco, and F. Saleri. *Numerical Mathematics*. Springer Verlag, New York, 2000.

[60] Rakesh. Inversion of spherically symetric potentials from boundary data for the wave equation. *Inverse Problems*, **14**:999–1007, 1998.

[61] Rakesh. Characterization of transmission data for webster's horn equation. *Inverse Problems*, **16**:L9–L24, 2000.

[62] Rakesh and P. Sacks. Impedance inversion from transmission data for the wave equation. *Wave Motion*, **24**:263–274, 1996.

[63] Roskoski, R. The ErbB/HER receptor protein–tyrosine kinases and cancer. *Biochem. Biophys. Res. Commun.*, **319**:1–11, 2004.

[64] Ross, J. S. and J. A. Fletcher. The HER–2/neu oncogene in breast cancer: prognostic factor, predictive factor, and target for therapy. *Oncologist*, **3**:237–252, 1998.

[65] Santosa, F. and H. Schwetlick. The inversion of acoustical impedence profile by method of characteristics. *Wave Motion*, **4**:99–110, 1982.

[66] Sharpe, F. R. and A. J. Lotka. A problem in age–distribution. *Phil. Mag.*, **21**:435–438, 1911.

[67] Skipper, H. E., F. M. Schnabel, and W. S. Wilcox. Experimental evaluation of potential anticancer agents. *Cancer Chemother. Rep.*, **35**:1–111, 1964.

[68] Slamon, D. J., W. Godolphin, L. A. Jones, J. A. Holt, S. G. Wong, D. E. Keith,

W. J. Levin, S.G. Stuart, J. Udove, and A. Ullrich. Studies of the HER–2/neu proto–oncogene in human breast and ovarian cancer. *Science*, **244**:707–712, 1989.

[69] Spector, N. L., W. Xia, H. Burris, H. Hurwitz, E. C. Dees, A. Dowlati, B. O'Neil, B. Overmoyer, P. K. Marcom, K. L. Blackwell, D. A. Smith, K. M. Koch, A. Stead, S. Mangum, M. J. Ellis, L. Liu, A. K. Man, T. M. Bremer, J. Harris, and S. Bacus. Study of the biologic effects of lapatinib, a reversible inhibitor of ErbB1 and ErbB2 tyrosine kinases, on tumor growth and survival pathways in patients with advanced malignancies. *J. Clin. Oncol.*, **23**:2502–2512, 2005.

[70] Spinelli, L., A. Torricelli, P. Ubezio, and B. Basse. Modelling the balance between quiescence and cell death in normal and tumour cell populations. *Math. Biosci.*, **202**:349–370, 2006.

[71] Sprague, B., R. L. Pego, D. A. Stavreva, and J. G. McNally. Analysis of binding reactions by fluorescence recovery after photobleaching. *Biophys. J.*, **86**:3473–3495, 2004.

[72] Stavreva, D. A. and J. G. McNally. Fluorescence recovery after photobleaching (FRAP) methods for visualizing protein dynamics in living mammalian cell nuclei. *Methods in Enzymology*, **375**:443–455, 2003.

[73] Symes, W. W. Impedance profile inversion via the first transport equation. *J. Math. Anal. Appl.*, **94**:435–453, 1983.

[74] Symes, W. W. Stability properties for the velocity inversion problem. In W. E. Fitzgibbon, editor, *Mathematical and Computational Methods in Seismic Exploration and Reservoir Modeling*, pages 128–157, Philadelphia, PA, 1986. SIAM.

[75] Tadi, M. Explicit method for inverse wave scattering in solids. *Inverse Problems*, **13**:509–521, 1997.

[76] Tardy, Y., J. L. McGrath, J. H. Hartwig, and C. F. Dewey. Interpreting photoactivated fluorescence microscopy measurements of steady–state actin dynamics. *Biophys. J.*, **69**:1674–1682, 1995.

[77] Thor, A. D., S. Liu, S. Edgerton, D. Moore, K. M. Kasowitz, C. C. Benz, D. F. Stern, and M. P. DiGiovanna. Activation (tyrosine phosphorylation) of ErbB–2 (HER–2/neu): a study of incidence and correlation with outcome in breast cancer. *J. Clin. Oncol.*, **18**:3230–3239, 2000.

[78] Troutman, J. *Variational Calculus with Elementary Convexity*. Springer Verlag, New York, 1983.

[79] Tubiana, M. The kinetics of tumour cell proliferation and radiotherapy. *Br. J. Radiol.*, **44**:325–347, 1971.

[80] Ubezio, P. Unraveling the complexity of cell cycle effects of anticancer drugs in cell populations. *Discrete Contin. Dyn. Syst. Ser. B*, **4**:323–335, 2004.

[81] von Hippel, P. H. and O. G. Berg. Facilitated target location in biological systems. *J. Biol. Chem.*, **264**:675–678, 1989.

[82] Waharte, F., C. M. Brown, S. Coscoy, E. Coudrier, and F. Amblard. A two-photon FRAP analysis of the cytoskeleton dynamics in the microvilli of intestinal cells. *Biophys. J.*, **88**:1467–1478, 2005.

[83] Walsh, J. B. An introduction to stochastic partial differential equations. In *École d'été de probabilités de Saint–Flour, XIV—1984*, number **1180** in Lecture Notes in Mathematics, pages 265–439, Berlin, 1986. Springer.

[84] Wang, S., A. Narasanna, M. Perez-Torres, B. Xiang, F. Wu, S. Yang, G. Carpenter, A. Gazdar, S. Muthuswamy, and C. Arteaga. HER2 kinase domain mutation results in constitutive phosphorylation and activation of HER2 and EGFR and resistance to EGFR tyrosine kinase inhibitors. *Cancer Cell*, **10**:25–38, 2006.

[85] Webb, G. F. *Theory of Nonlinear Age–Dependent Population Dynamics*. Marcel Dekker, New York, 1985.

[86] Weiss, M. Challenges and artifacts in quantitative photobleaching experiments. *Traffic*, **5**:662–671, 2004.

[87] Yang, F., L. G. Moss, and G. N. Phillips. The molecular structure of green fluorescent protein. *Nature Biotechnol.*, **14**:1246–1251, 1996.

[88] Yarden, Y. and M. X. Sliwkowski. Untangling the ErbB signalling network. *Nat. Rev. Mol. Cell Biol.*, **2**:127–137, 2001.

[89] Yokoe, H. and T. Meyer. Spatial dynamics of GFP–tagged proteins investigated by local fluorescence enhancement. *Nature Biotechnol.*, **14**:1252–1256, 1996.

[90] Zhdanov, M. S. *Geophysical Inverse Theory and Regularization Problems*. Elsevier, Amsterdam, 2002.